

## Controls on Eurasian coastal sea ice formation, melt onset and decay from ERS scatterometry: regional contrasts and effects of river influx

K. E. FREY\*, L. C. SMITH and D. E. ALSDORF

Department of Geography, University of California, Los Angeles, CA, USA

(Received 21 May 2002; in final form 27 January 2003)

**Abstract.** Regional and local patterns in the formation, melt onset and disappearance of coastal first-year sea ice (FYI) are observed in the Eurasian Arctic using the C-band (5.3 GHz) European Remote Sensing Satellite (ERS) radar scatterometers. Near-daily time-series (1991–1999) of the radar backscatter coefficient normalized to an incident angle of  $40^\circ$  ( $\sigma_{40}^0$ ) and the backscatter–incident angle relationship ( $B$ ) are examined for test sites near the Severnaya Dvina, Mezen, Pechora, Ob', Yenisei, Khatanga, Lena, Indigirka and Kolyma rivers. Melt onset of the sea ice surface is associated with abrupt changes in  $\sigma_{40}^0$ , with values converging towards  $\sim -17$  dB. As such, whether backscatter increases or decreases at melt onset is largely determined by contrast with pre-melt backscatter levels. The presence or absence of FYI is designated from low or high values of  $B$ , respectively, whereas the addition of an anisotropy criterion further improves discrimination of FYI from open water. A strong regional pattern is seen in the daily temporal variability of both melt onset and ice cover, with maximum variability in the Barents and Kara seas and decreasing variability eastward. Similarly, significant contrasts in the seasonal duration of ice cover are found between western and eastern sites. Seasonal ice cover persists  $\sim 144$  days for sites in the Barents Sea, but  $\sim 293$  days for sites farther east in the East Siberian Sea. We speculate that our observed west–east contrasts are due to North Atlantic modulation of salinity, air temperature and cyclone density. Rivers also exert a local effect on ice cover, causing earlier formation ( $\sim 4$  days) and earlier disappearance ( $\sim 17$  days) near river mouths. The hydrological influence of rivers is potentially strong in the Kara, Laptev and East Siberian seas, but weak or absent in the Barents Sea.

### 1. Introduction

The response of sea ice to climate change is a critical topic in Arctic science, as both model results (Ramanathan 1988, Manabe *et al.* 1991, Keeling *et al.* 1996) and the observational record (e.g. Cavalieri *et al.* 1997, Johannessen *et al.* 1999, Parkinson *et al.* 1999, Vinnikov 1998, Hilmer and Lemke 2000) indicate a broad warming trend at high latitudes. Continued warming in the Arctic is expected to have a significant impact on the continental shelves of the Arctic Ocean (Grebmeier

---

\*Corresponding author; e-mail: frey@ucla.edu

*et al.* 1998), most of which are seasonally covered by coastal first-year sea ice (FYI). Eurasia, in particular, contains the Earth's largest area of contiguous shelf and is also a major source of hemispheric sea ice (Forman and Johnson 1998). However, regional and local controls on FYI cover must first be assessed before the effects of global-scale climate change on Eurasian shelf ice can be identified or predicted.

Some of the greatest regional influences in the Arctic are those driven by North Atlantic circulation. North Atlantic waters strongly influence the import of heat, mass and salinity into the Arctic Ocean, with important consequences for arctic climatology, sea ice stability, and poleward heat flux. Northward transport of equatorial water raises North Atlantic surface water temperatures  $\sim 4^{\circ}\text{C}$  compared to similar latitudes in the Pacific (Levitus 1982, Weaver *et al.* 1999), warming the winter climate of north-western Europe (Hall and Bryden 1982, Roemmich and Wunsch 1985). North Atlantic sea surface temperatures regulate surface air pressure patterns, the strength and location of westerlies, and cyclone tracks, all impacting surface climate over northern Eurasia. Surface temperature and precipitation anomalies in northern Eurasia have also been attributed to North Atlantic influences, in both the instrumental data record of the last century (Peng and Mysak 1993, Perlwitz and Graf 1995, Rogers and Mosley-Thompson 1995, Griffies and Bryan 1997, Halpert and Bell 1997, Hurrell and VanLoon 1997, Clark *et al.* 1999, Ye 2000) and proxy palaeoclimate data throughout the Holocene (Lehman and Keigwin 1992, Cook *et al.* 1998, MacDonald *et al.* 2000a, b, Snyder *et al.* 2000). Atlantic modulation is thought to impart inter-decadal variability between two major climate regimes across the Arctic (Proshutinsky and Johnson 1997, Polyakov *et al.* 1999, Proshutinsky *et al.* 1999), triggering a dominance of either cyclonic or anticyclonic atmospheric circulation. In the past 30 years, North Atlantic impacts on Arctic atmospheric circulation have shown large deviations from normal with a cyclonic pattern of circulation persisting over the polar region, resulting in unusually low pressure, strong subpolar westerlies and warm high-latitude temperatures over land (Kerr 1999, Serreze *et al.* 2000). It has been argued that this has further enhanced North Atlantic climatic influence in northern Eurasia (Hurrell 1995, 1996, Hurrell and VanLoon 1997, Häkkinen and Geiger 2000). The recent persistence of Arctic cyclone activity has also been linked to relatively large reductions (particularly along the Siberian sector) in Northern Hemisphere sea ice cover (Serreze *et al.* 1995a, Maslanik *et al.* 1996).

At the local scale, river influx also affects the formation and decay of coastal FYI. A river-sea ice interaction model (Searcy *et al.* 1996) suggests that river discharge provides half of the energy needed to melt ice cover in the nearshore region. River floods may also flow out over the sea ice surface (Matthews and Stringer 1984), adding thermal energy to the ice and also depositing sediments, thereby reducing ice albedo (Walker 1998). Thermal input from the Mackenzie River was shown to accelerate local sea ice disappearance by up to 14 days (Dean *et al.* 1994, Searcy *et al.* 1996), although Dean *et al.* (1994) determine that ice removal near the delta is actually initiated two months earlier than elsewhere. In the Laptev Sea, Bareiss *et al.* (1999) report ice disappearance roughly three weeks earlier in the vicinity of the Lena River, attributed to both thermal heat input and overflowing of land-fast ice. Freshwater runoff also plays a fundamental role in promoting sea ice formation on the shelf seas and the Arctic Ocean (Barry *et al.* 1993), where positive correlations between ice and river discharge anomalies are

found at lags of 10–12 months (Holt *et al.* 1984, Manak and Mysak 1989). Approximately 75% of the total terrestrial freshwater flux to the Arctic Ocean originates in continental Eurasia, where  $\sim 70\%$  of this Eurasian runoff is derived from the Ob', Yenisei and Lena rivers alone (Carmack 1990, Gordeev *et al.* 1996). Hence, the effects of river influx on Eurasian coastal FYI may be particularly evident.

The potential value of satellite radar scatterometer data in sea ice studies has been recognized since early applications of Seasat data (Drinkwater and Carsey 1991). In the past decade, many studies have used data from the C-band European Remote Sensing Satellite (ERS) scatterometers (Gohin and Cavanié 1994, Cavanié 1998, Drinkwater *et al.* 1998, Grandell *et al.* 1999, Drinkwater and Liu 2000, Haas 2001), the Ku-band National Aeronautics and Space Administration (NASA) scatterometer (NSCAT) (Yueh and Kwok 1998, Ezraty and Cavanié 1999a, Long and Drinkwater 1999, Remund and Long 1999, Forster *et al.* 2001), or a combination of the two (Ezraty and Cavanié 1999b, Remund *et al.* 2000) to investigate sea ice melt onset, classification and extent in the Arctic and Antarctic. Few of these scatterometer studies, however, focus specifically on the dynamics of FYI and most investigate sea ice properties based on backscatter signatures only (e.g. Cavanié 1998, Drinkwater *et al.* 1998, Ezraty and Cavanié 1999b, Drinkwater and Liu 2000, Haas 2001). The Centre ERS d'Archivage et de Traitement (CERSAT) French Processing and Archiving Facility (F-PAF) offers weekly sea ice products of ERS backscatter (<http://www.ifremer.fr/cersat/>) from 1991–1996. Sheng *et al.* (2002) provide one-day, three-day and seven-day products of ERS backscatter in the Arctic from 1991–2000. The incident angle dependence of backscatter is also shown to be valuable in sea ice applications. Gohin and Cavanié (1994) present a first use of the ERS backscatter–incident angle relationship for sea ice detection. Other backscatter–incident angle dependence algorithms have been presented with varying success for ERS (e.g. Grandell *et al.* 1999, Remund *et al.* 2000). CERSAT additionally offers weekly sea ice products (1991–1996) of the backscatter–incident angle derivative at  $28^\circ$ .

In this study, we present a scatterometer algorithm similar to that used by Grandell *et al.* (1999) to generate scatterometer data products with near-daily temporal resolution. The algorithm uses radar backscatter, the slope of the backscatter–incident angle relationship and anisotropy to infer the presence of sea ice and the occurrence of melting on its overlying snow cover. Nine years of ERS scatterometer data are used to (1) infer the extent of North Atlantic climatic influences on Eurasian coastal FYI, and (2) examine effects of river influx on coastal FYI in order to separate local variability from larger regional patterns. Both goals are addressed by examining spatial patterns in sea ice formation, melt onset and disappearance derived from the scatterometer data. The timing of these events is determined for 18 sites spanning the northern Eurasian coast near the Severnaya (Sev.) Dvina, Mezen, Pechora, Ob', Yenisei, Khatanga, Lena, Indigirka and Kolyma rivers, with one 'river-distal' (a) and one 'river-proximal' (b) site per river (figure 1). Scatterometer observations of the 18 sites are compared with sea ice concentration estimates derived from Special Sensor Microwave/Imager (SSM/I) passive microwave satellite data, meteorological station air temperatures and river discharge records.

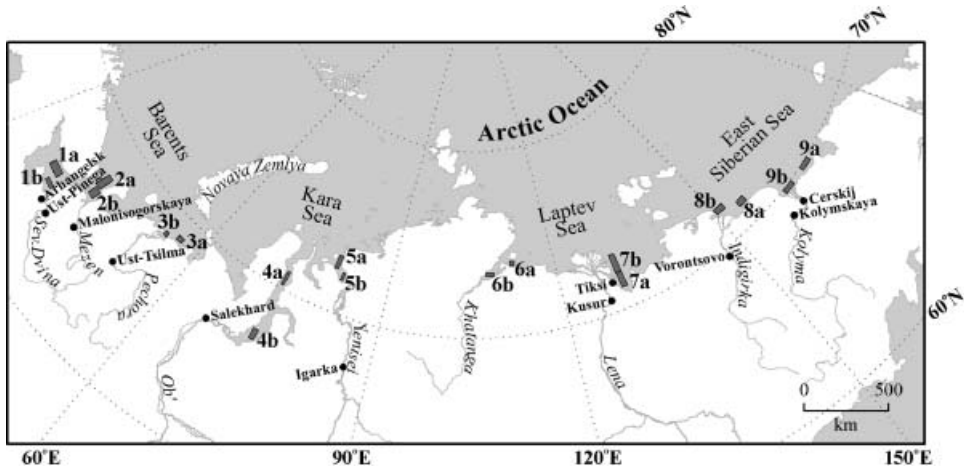


Figure 1. Location of study areas. Scatterometer and passive microwave time-series are averaged over the rectangular areas labelled 1–9, with one river-distal site (a) and one river-proximal site (b) for each of the nine rivers studied. River-proximal sites are located 50–250 km from associated river mouths. River-distal sites are located an additional 80–400 km away from proximal sites. For sites 4, 5 and 6, irregular coastlines constrained site placement, but in all cases, distal sites were selected so as to minimize river influence. Circles represent meteorological and discharge stations used in this study.

## 2. Data and methods

### 2.1. ERS scatterometry

The ERS wind scatterometers operate at C-band (5.3 GHz), with VV polarization (vertically sent and received radar pulses), incident angles of 18–59°, an illuminated swath width of 500 km, an along-track and cross-track spatial resolution of 50 km, and a processed pixel spacing of 25 km (ESA 1993). Data are available from both ERS-1 (1991–1996) and ERS-2 (1996–2001). Collection of scatterometer data was suspended until further notice in January 2001, owing to the failure of a digital Earth sensor and subsequent failure of a gyroscope. Scatterometry offers distinct advantages over optical systems owing to its independence from sunlight and cloud conditions and more frequent coverage (near-daily at Arctic latitudes) than synthetic aperture radar (SAR). For each imaged ground element, the scatterometer measures the backscatter coefficient  $\sigma^0$  of a target from three directions, looking 45° (fore-beam), 90° (mid-beam) and 135° (aft-beam) with respect to the satellite flight direction. The fore- and aft-beam obtain data at nearly identical incident angles (ranging from 25–59°), whereas the mid-beam obtains data at incident angles 7–12° smaller (ranging from 18–47°). Therefore, for each imaged ground element, three independent  $\sigma^0$  values are obtained using three look directions at two different incident angles. Although the primary purpose of the ERS scatterometers is to derive ocean wind products, their frequent global coverage over land also allows investigation of soil, vegetation, snow and ice dynamics at regional to continental scales (Wismann 1998). Here, we use scatterometer data to investigate three distinct coastal FYI events: melt onset, sea ice decay and sea ice formation. Exploratory methodologies for detecting these states are presented in the following two sections.

## 2.2. Radar backscatter and melt onset

With the arrival of above freezing air temperatures, the initial appearance of liquid water at the surface of the snow pack overlying sea ice is easily detected as an abrupt change in radar backscatter. Most commonly, backscatter is strongly reduced (e.g. Winebrenner *et al.* 1994, Kwok *et al.* 1998, Yueh and Kwok 1998, Long and Drinkwater 1999, Drinkwater and Liu 2000, Forster *et al.* 2001, Haas 2001), though backscatter increases are also reported (e.g. Barber *et al.* 1992, Forster *et al.* 2001). This effect stems from an abrupt change in the scattering properties of snow. Backscatter response from dry snow is dominated by volume scattering. However, with the presence of liquid water, radar penetration depth decreases considerably and surface scattering becomes dominant (Hall 1998). The formation of even a thin layer of moist snow as temperatures rise above freezing provides sufficient change in microwave signatures to detect this event (e.g. Shokr and Barber 1994, Winebrenner *et al.* 1994, Barber *et al.* 1998).

In order to use scatterometer data to detect melt onset, incident angle effects on backscatter must first be corrected. The correction is needed to mitigate backscatter variations due solely to radar incident angle ( $\theta$ ). Three independent backscatter coefficients ( $\sigma^0_f$ ,  $\sigma^0_m$ ,  $\sigma^0_a$ , where  $f$ ,  $m$  and  $a$  are fore-beam, mid-beam and aft-beam, respectively), each with an associated incident angle ( $\theta_f$ ,  $\theta_m$ ,  $\theta_a$ ), are simultaneously obtained for each imaged ground element, or pixel. Incident angle effects on  $\sigma^0$  may be corrected for each pixel using a signal linearization method (e.g. Kennett and Li 1989, Long *et al.* 1993), which assumes a linear dependence of  $\sigma^0$  upon  $\theta$ . This dependence is calculated by least-squares fit through the three simultaneously obtained data points. This linear fit is then used to compute the  $\sigma^0$  value predicted for a  $\theta$  of  $40^\circ$ . The result, designated  $\sigma^0_{40}$ , is corrected for backscatter variations caused solely by incident angle. Because each of our study sites contains a number of pixels (ranging from 4 to 25),  $\sigma^0_{40}$  pixel values within each site were averaged, yielding a nine-year time-series of near-daily  $\sigma^0_{40}$  for each of the 18 study sites.

## 2.3. Dependence of radar backscatter on incident angle

The dependence of backscatter on incident angle can be approximated by assuming a linear fit through the three  $\sigma^0$  and  $\theta$  pairs acquired for each pixel, as described above. In addition to being used to derive values of  $\sigma^0_{40}$ , the slope of this best-fit line also contains useful information about surface scattering properties and can be described as (Gohin and Cavanié 1994):

$$\sigma^0 = A + B\theta \quad (1)$$

where backscatter ( $\sigma^0$ ) is measured in dB, the intercept ( $A$ ) in dB, the slope parameter ( $B$ ) in dB degree<sup>-1</sup> and the incident angle ( $\theta$ ) in degrees. Like backscatter,  $B$  is influenced by imaging geometry. The ERS satellites have a global repeat-cycle period (i.e. a particular target is imaged with identical orbital geometry) of 35 days. However, the large swath width of scatterometer data and orbital convergence at high latitudes cause the sites in this study to be imaged almost daily, but with differing viewing geometries. Thus, the target is imaged at different positions within the image swath, resulting in variable incident angles. This variation in incident angle from one overlapping orbit to the next should not be confused with the simultaneous variation in incident angle (between  $\theta_f$ ,  $\theta_m$  and  $\theta_a$ ) described in §2.1. Therefore, incident angle variations may be separated into two

categories: small variations ( $\sim 0\text{--}12^\circ$ ) between  $\theta_f$ ,  $\theta_m$  and  $\theta_a$ , and potentially large variations ( $\sim 0\text{--}32^\circ$ ) caused by imaging geometry. Here, the latter effect ('orbital incident angle' or  $\theta_{orb}$ ) is approximated as the average incident angle of the three beams:

$$\theta_{orb} = (\theta_f + \theta_m + \theta_a) / 3 \quad (2)$$

Thus,  $B$  can be roughly thought of as the local derivative of the backscatter–incident angle relationship at  $\theta_{orb}$ .

The  $\theta_{orb}$  parameter exerts a strong effect upon  $B$  (figure 2). In winter,  $B$  displays little dependence on  $\theta_{orb}$ , with most values falling between  $-0.1$  and  $-0.4$  across all  $\theta_{orb}$  values (i.e. across the entire swath width or range of the scatterometer). In summer, the magnitude of  $B$  is high at small  $\theta_{orb}$  (near-range) and low at large  $\theta_{orb}$  (far-range). However, at high  $\theta_{orb}$ ,  $B$  converges to similar values year-round (figure 2). This phenomenon creates an ambiguity in deciphering  $B$  at larger  $\theta_{orb}$  values. Here, we employ a first-order correction designed to reduce the dependence of  $B$  on  $\theta_{orb}$  while still retaining all available data. The procedure is as follows (figure 3). (1) For each site,  $B$  values (figure 3(a)) are separated into three categories: near-range ( $\theta_{orb} < 33^\circ$ ) (figure 3(b)), mid-range ( $33^\circ \leq \theta_{orb} < 43^\circ$ ) (figure 3(c)) and

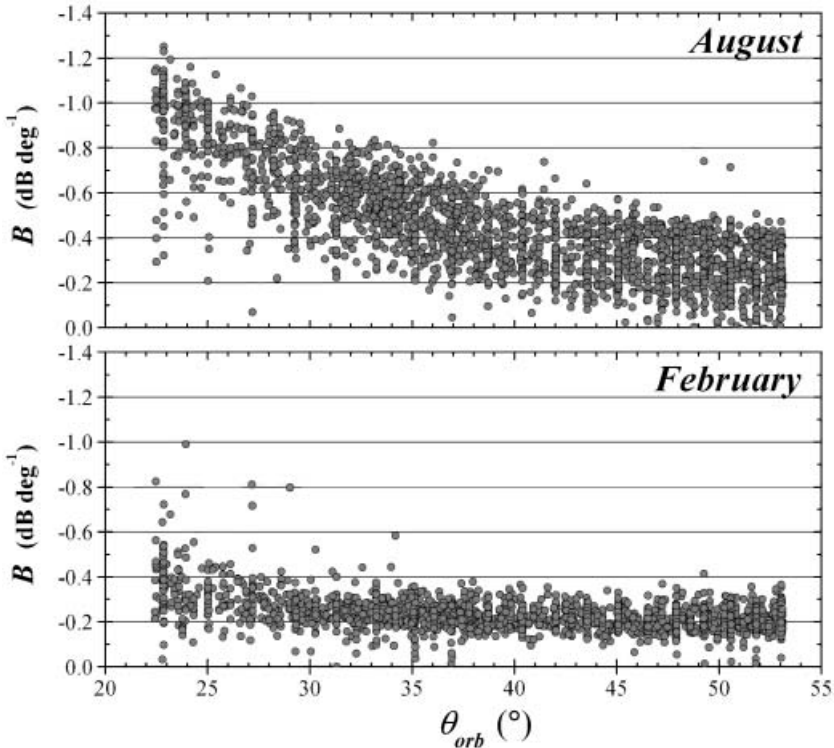


Figure 2. Correlation of the slope parameter ( $B$ ) and orbital incident angle ( $\theta_{orb}$ ) for all 18 sites. Dependence of  $B$  on  $\theta_{orb}$  is strong in August but weak in February.  $B$  values converge to similar (low) values at high  $\theta_{orb}$  year-round, creating an ambiguity in interpreting the radar return.

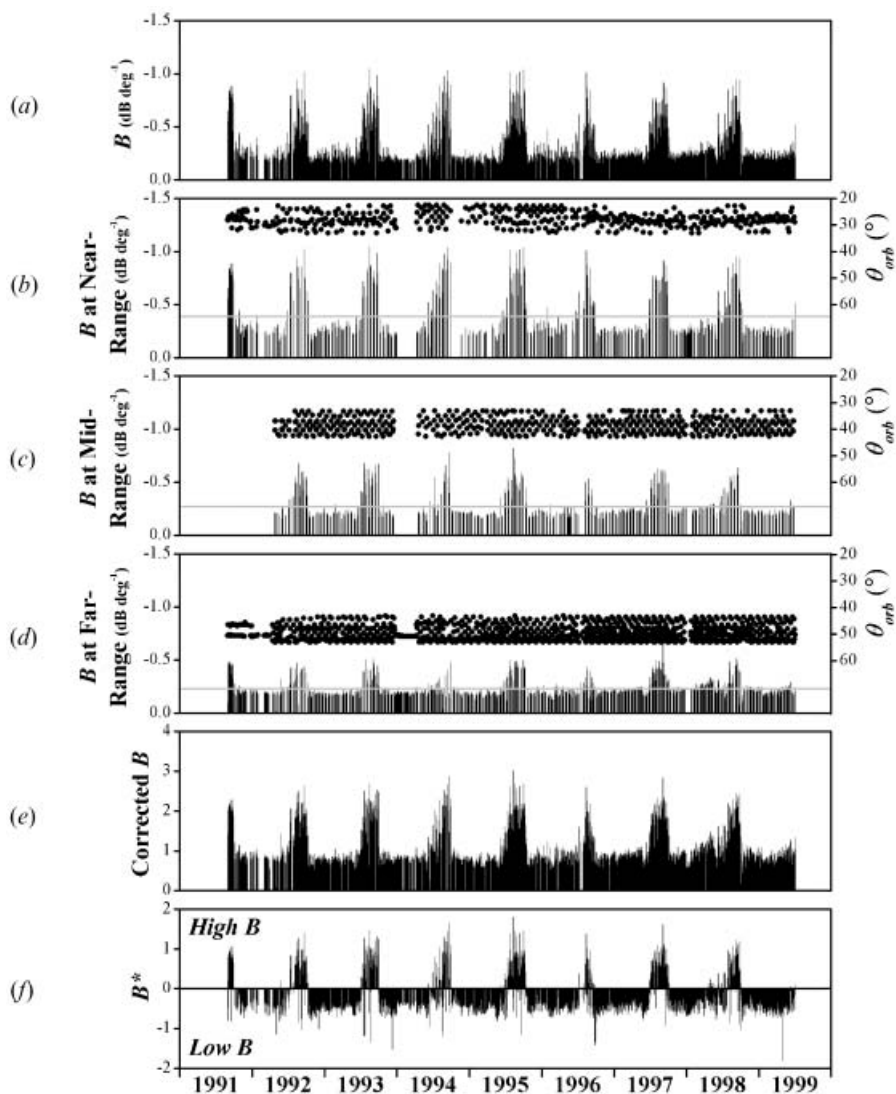


Figure 3. Procedure used to convert  $B$  to the final normalized and corrected  $B^*$  used to extract dates of sea ice formation and decay. Data from site 9b are used in this example. (a)  $B$  values. (b)  $B$  values separated into categories of  $B$  at near-range ( $\theta_{orb} < 33^\circ$ ); (c)  $B$  at mid-range ( $33^\circ \leq \theta_{orb} < 43^\circ$ ); and (d)  $B$  at far-range ( $\theta_{orb} \geq 43^\circ$ ). (e) Corrected and collated  $B$  values. (f) Final  $B^*$  time-series. See §2.3 for a more detailed description of this procedure. Grey lines represent series means.  $\theta_{orb}$  values are represented as dots and are scaled at right.

far-range ( $\theta_{orb} \geq 43^\circ$ ) (figure 3(d)). This roughly corresponds to a three-day cycle of scatterometer imaging (e.g. where sites are imaged at near-range on day one, mid-range on day two and far-range on day three). (2) Time-series for each category (figure 3(b, c, d)) are normalized (divided by the series mean). (3) These three normalized series are collated into one dataset, yielding a new, corrected time-series for which first-order effects of viewing geometry on  $B$  have been removed

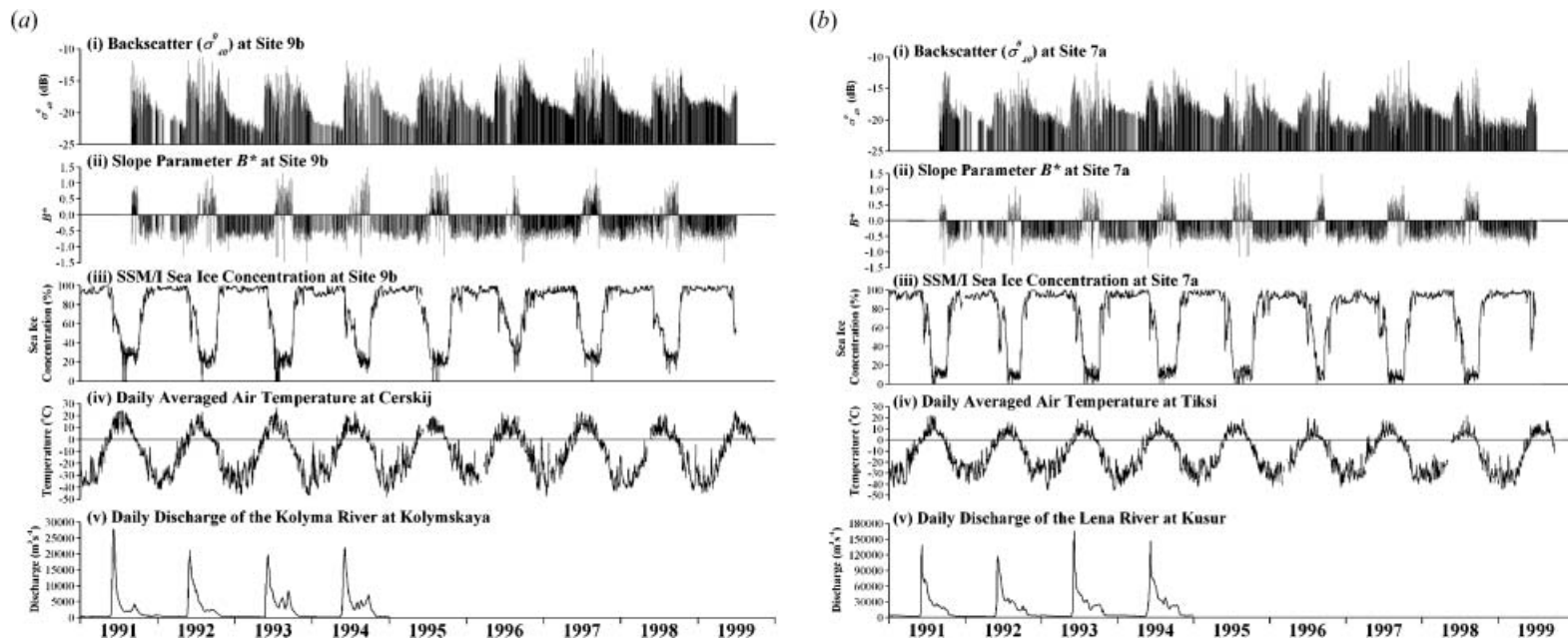


Figure 4. Time-series compilations for test sites near (a) Kolyma, (b) Lena and (c) Sev. Dvina rivers. Each compilation includes (i) normalized radar backscatter ( $\sigma_{40}^0$ ), (ii)  $B^*$ , (iii) SSM/I sea ice concentration, (iv) daily averaged air temperature and (v) available daily discharge.

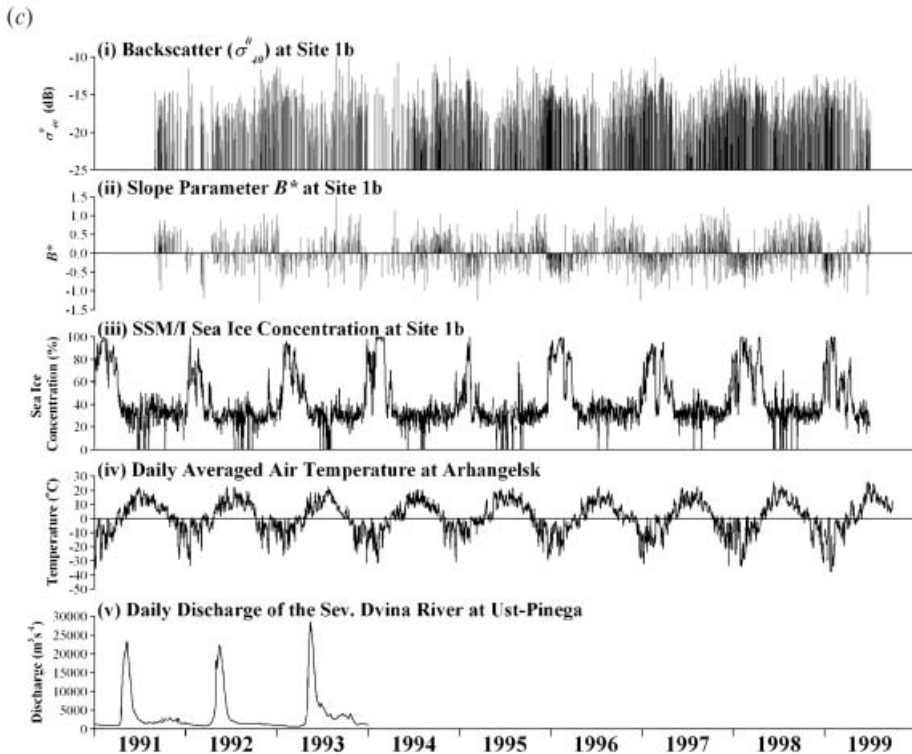


Figure 4(c).

(figure 3(e)). (4) An empirically derived constant is subtracted from this corrected series to facilitate direct comparison between sites. This constant is defined as two-thirds of the difference between averaged August and averaged February corrected  $B$  values within each dataset. This produces a final series of  $B^*$  in which positive values represent high  $B$  and negative values represent low  $B$  (figure 3(f)), making seasonal transitions between negative and positive readily apparent. The empirically derived ‘two-thirds’ constant allows for the best separation of summer and winter  $B$  values by efficiently preventing the contamination of probable summer  $B$  values from occurring during winter months and vice versa. The final  $B^*$  time-series is smoothed with a three-day filter for subsequent analyses.

#### 2.4. Passive microwave, meteorological station air temperature, and river discharge time-series

Scatterometer  $\sigma_{40}^0$  and  $B^*$  time-series are compared with SSM/I Daily Polar Gridded Sea Ice Concentrations, meteorological station air temperatures and river discharge records (figure 1, figure 4(a), (b), (c)). SSM/I-derived sea ice concentrations are based on the NASA Team Algorithm and provided by the EOS Distributed Active Archive Center (DAAC) at the National Snow and Ice Data Center, University of Colorado, Boulder, CO (Cavalieri *et al.* 1999). Here, the  $25 \text{ km} \times 25 \text{ km}$  sea ice concentration data are spatially averaged within the same study sites defined for the scatterometer time-series (sites 1–9). Three-hourly air

temperature data are obtained from the National Climatic Data Center (NCDC) at Arhangelsk, Tiksi and Cerskij and converted into daily averaged values. Daily discharge records from stations at Ust-Pinega, Malonisogorskaya, Oksino, Salekhard, Igarka, Kusur, Vorontsovo and Kolymskaya are obtained from the Global Runoff Data Centre (GRDC) in the Federal Institute of Hydrology, Germany, with records extending at latest to 1994.

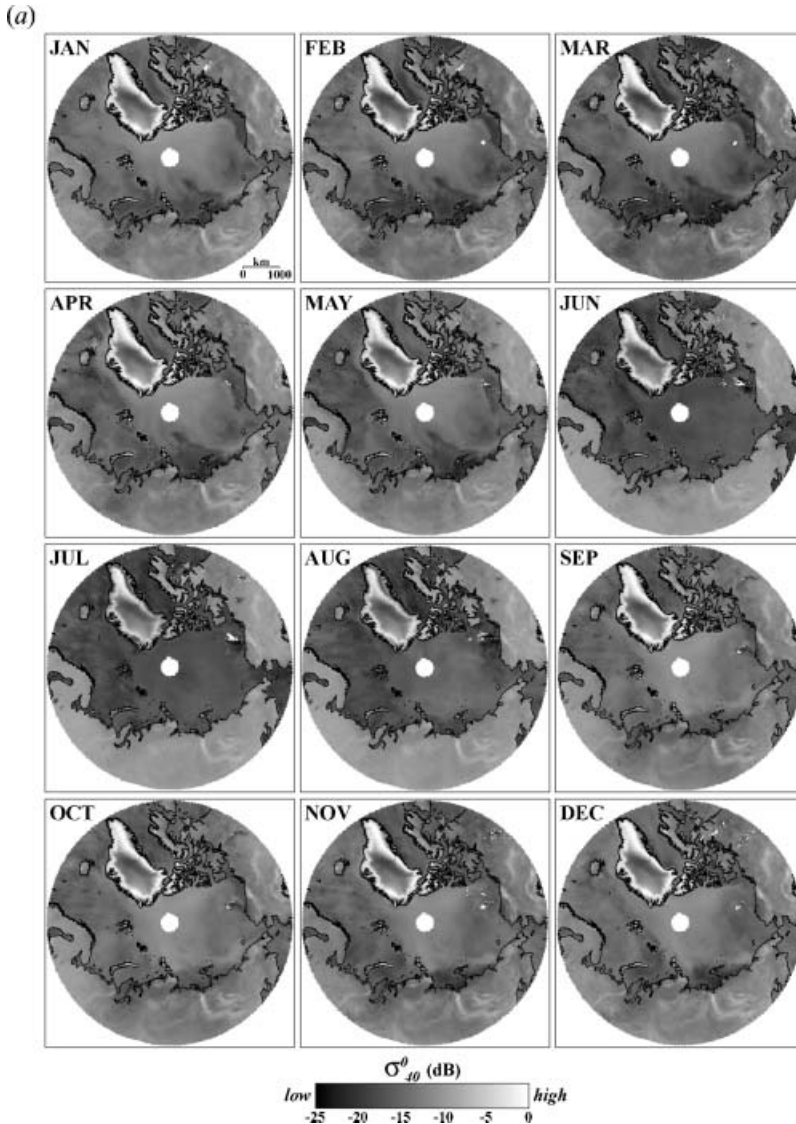


Figure 5. (a) Monthly-averaged ERS scatterometer  $\sigma_{40}^0$  maps of the Arctic from 60–90° N. Most commonly, melt onset (June) is associated with  $\sigma_{40}^0$  increases over first-year ice (FYI). However,  $\sigma_{40}^0$  decreases are found over FYI in the Barents Sea and over multi-year ice (MYI) farther north. (b) Monthly-averaged ERS scatterometer  $B$  maps of the Arctic from 60–90° N. High magnitude  $B$  values (open water) are found along the Eurasian coastline in summer months, followed by low magnitude  $B$  values (ice cover) in winter months.

### 3. Results

#### 3.1. Timing of melt onset, sea ice decay and sea ice formation

Scatterometer  $\sigma_{40}^0$  and  $B^*$  time-series show some striking correlations with daily averaged air temperature and SSM/I sea ice concentration data (figure 4(a), (b), (c)). At eastern sites such as 9b and 7a, sharp increases in  $\sigma_{40}^0$  (figure 4(a)(i), (b)(i)) are associated with above-freezing air temperatures (figure 4(a)(iv), (b)(iv)). The spatial pattern of increased brightness over FYI caused by melt onset can be seen in figure 5(a). However, at western sites such as 1b, above-freezing air temperatures (figure 4(c)(iv)) correspond to a decrease in  $\sigma_{40}^0$  (figure 4(c)(i)). This signature is

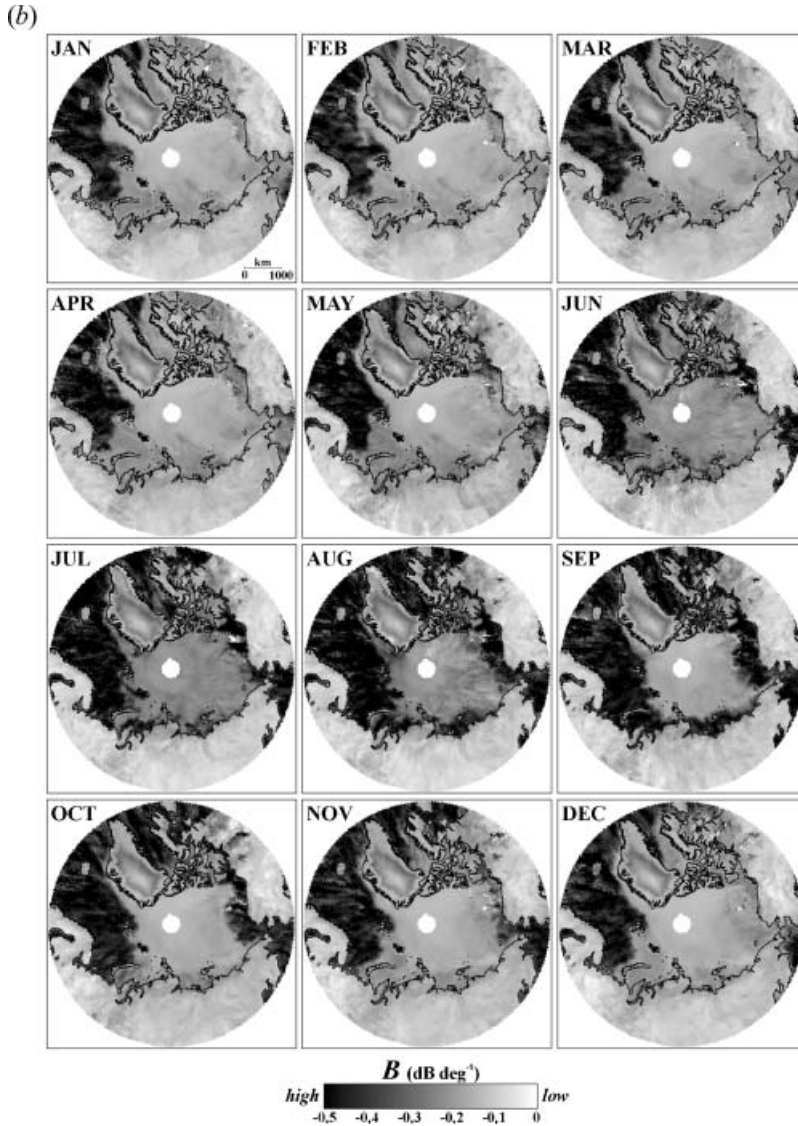


Figure 5(b).

noisy, though, and much less robust than the signatures at sites 7a and 9b. Summer  $\sigma_{40}^0$  values fluctuate widely for all sites, as is typical for open water conditions. Nevertheless, the arrival of above-freezing temperatures (melt onset) is associated with an abrupt increase or decrease in  $\sigma_{40}^0$ . Time-series of  $\sigma_{40}^0$  are constructed for each of the 18 sites, by subtracting the nine-year  $\sigma_{40}^0$  mean from each  $\sigma_{40}^0$  value, then selecting the first date of two consecutive  $\sigma_{40}^0$  values above or below this mean. This allows consistent detection regardless of whether individual sites display increased or decreased backscatter in response to melt onset (figure 6).

Backscatter alone cannot be used to detect the presence of sea ice because wet and/or rough FYI can yield the high backscatter signatures also seen over wind-roughened water. In turn, dry and smooth FYI can yield low backscatter signatures also seen over calm water. However, the dependence of backscatter on incident angle ( $B$ ) does seem to be sensitive to the presence or absence of sea ice. High  $B$  values are found along the Eurasian coastline in summer months, followed by low  $B$  values in winter months when air temperatures again fall below freezing (figure 5(b)). This pattern can also be seen in  $B^*$  time-series (figure 4(a)(ii), (b)(ii), (c)(ii)) that are negatively correlated with SSM/I sea ice concentrations (figure 4(a)(iii), (b)(iii), (c)(iii)). Positive  $B^*$  values are associated with the absence of sea ice, whereas negative  $B^*$  values are associated with the presence of sea ice. Annual transitions from positive to negative values also correlate well with the persistence of below-freezing air temperatures (figure 4(a)(iv), (b)(iv), (c)(iv)). These transitions in  $B^*$  are attributed to sea ice formation. Conversely, the annual transitions in  $B^*$  from negative to positive values are interpreted as the occurrence of sea ice decay. Although the exact physical state of the sea ice during these transitions is unknown, this study uses the terms sea ice decay and formation as technical terms to describe when scatterometer data first show a dominant signal of either summer or winter conditions, respectively.

Two physical mechanisms driving the observed variability of the slope parameter  $B$  are surface scattering from open water and volume scattering from

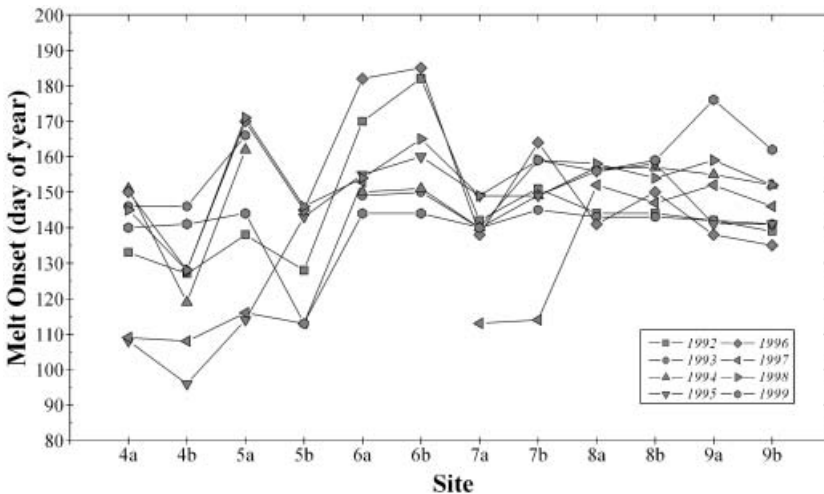


Figure 6. Inter-annual variability in melt onset, sites 4–9. Melt onset could not be determined for sites 1–3. Central sites show highest inter-annual variability.

ice and snow. The scattering behaviour of radar waves from rough and smooth surfaces can be quantified through the use of scattering models that relate surface roughness to radar backscatter (e.g. Ulaby *et al.* 1982). Surface scattering from a smooth water surface produces high backscatter at small incident angles but decreases sharply with increasing incident angle (yielding high  $B$  values). Volume scattering from ice and snow displays little dependence on incident angle (yielding low  $B$  values). Therefore, high  $B$  values represent open water and low  $B$  values represent sea ice. Following our correction and normalization procedure of  $B$  time-series (§2.3.), we ‘flag’ sea ice or open water conditions from negative or positive  $B^*$  values, respectively (e.g. figure 7).

Additional variability in  $B$  is introduced by the dependence of backscatter on the azimuthal look direction of the three scatterometer beams (note the summer variability in  $B^*$  time-series, figure 4(a)(ii), 4(b)(ii), 4(c)(ii)), an effect known as azimuthal modulation (e.g. Early and Long 1997). The magnitude of this effect can also help to differentiate sea ice from open water. With the incident angle dependence of backscatter removed (§2.2.), backscatter returns are relatively similar in all directions over sea ice and the azimuthal dependence of backscatter can be assumed to be negligible ( $< 1$  dB) (Early and Long 1997). The azimuthal dependence of backscatter over open water, however, can be extremely significant. This behaviour is often described as the isotropic behaviour of sea ice and the anisotropic behaviour of open water. The latter, caused by unidirectional wind forcing of ocean waves, is what enables derivation of ocean wind fields from scatterometer data. Wind-roughened water surfaces may cause enhanced backscatter in only one azimuthal direction, resulting in low  $B$  values similar to those of sea ice. Relatively calm waters, however, result in high  $B$  values. This azimuthal dependence of backscatter and resulting potential variability of  $B$  over open water surfaces is apparent in the greater spread of  $B$  values for a given  $\theta_{orb}$  during August than during February (figure 2).

Owing to the isotropic scattering nature of sea ice surfaces, wintertime  $B^*$  values robustly detect sea ice (figure 4a(ii), (b)(ii), (c)(ii)). Conversely, we find that the anisotropic nature of open water surfaces can lead to erroneous detection of sea ice in summer. To mitigate this result, we added the use of an anisotropy criterion to our  $B^*$  time-series. Because  $\theta_f$  and  $\theta_a$  are nearly identical and have azimuths  $90^\circ$  apart, any azimuthal modulation of the imaged surface will be apparent in the backscatter returns of these two beams ( $\sigma_f^0$  and  $\sigma_a^0$ ). Therefore, any difference in  $\sigma_f^0$  and  $\sigma_a^0$  is a measure of surface scattering anisotropy:

$$\sigma_{f-a}^0 = \left| \sigma_f^0 - \sigma_a^0 \right| \quad (3)$$

For the 18 sites in this study,  $\sigma_{f-a}^0$  ranges from  $\sim 0$ –2 dB (low anisotropy) over sea ice and from  $\sim 0$ –7 dB (high anisotropy) over open water. Following smoothing with a three-day filter,  $\sigma_{f-a}^0$  values greater than 2 dB are considered water, effectively overriding erroneous  $B^*$ -derived sea ice flags. Figure 7 presents the derived time-series of the presence or absence of coastal FYI for all 18 sites. From these time-series, dates of sea ice decay are identified as the first day when four of six consecutive flags are designated water. Dates of sea ice formation are identified as the first day following the last four of six consecutive water flags within the season. Because the datasets are smoothed with a three-day filter, one outlying  $B^*$  value could result in three very high or very low adjacent values. Therefore,

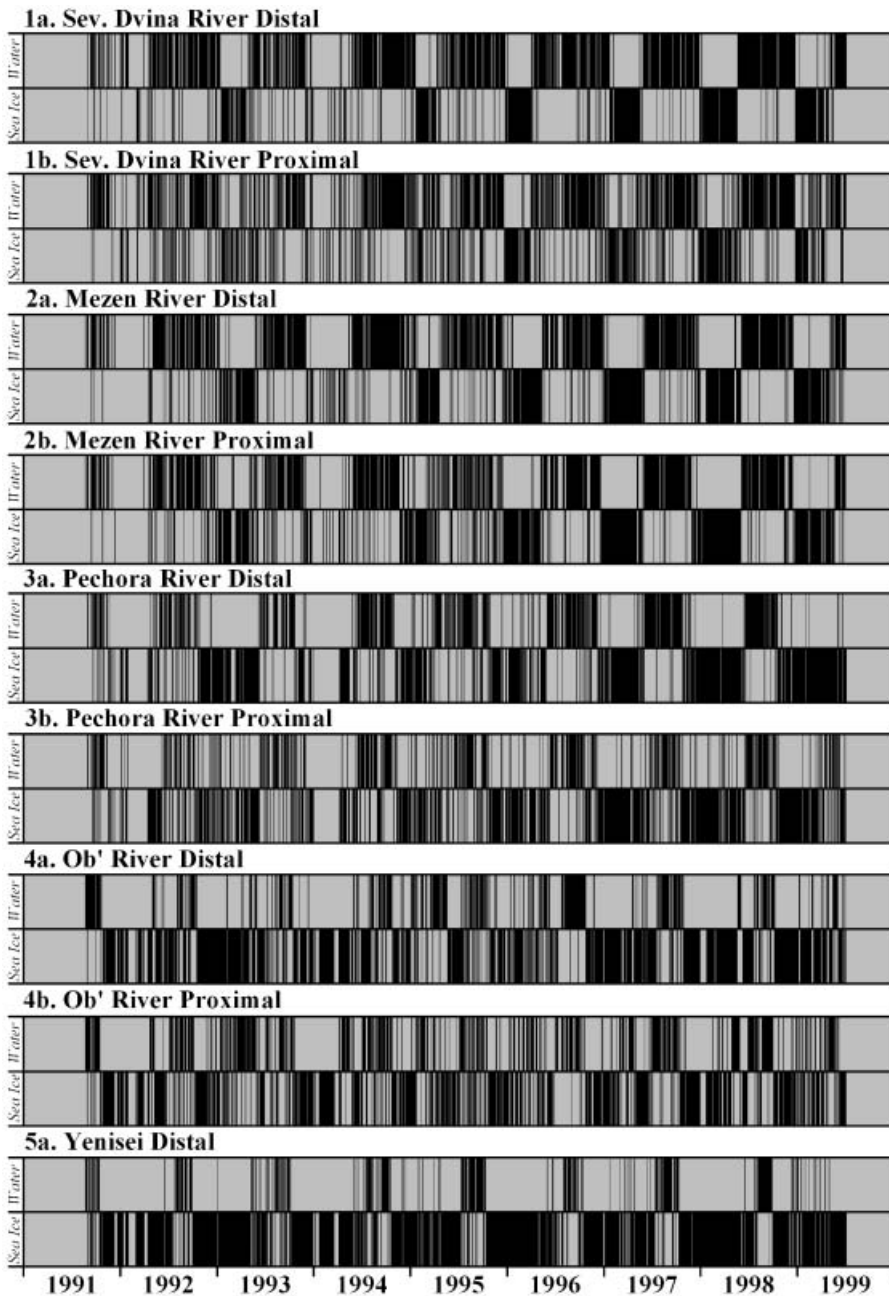


Figure 7. Flags of open water and sea ice for all 18 sites, classified from  $B^*$  time-series and fore-beam–aft-beam backscatter differences ( $\sigma_{f-a}^0$ ). Each day contains only one water or ice flag (high data density of these plots does not always permit individual flags to be resolved). Western sites are more variable than eastern sites. The annual length of ice cover also increases significantly from west to east.

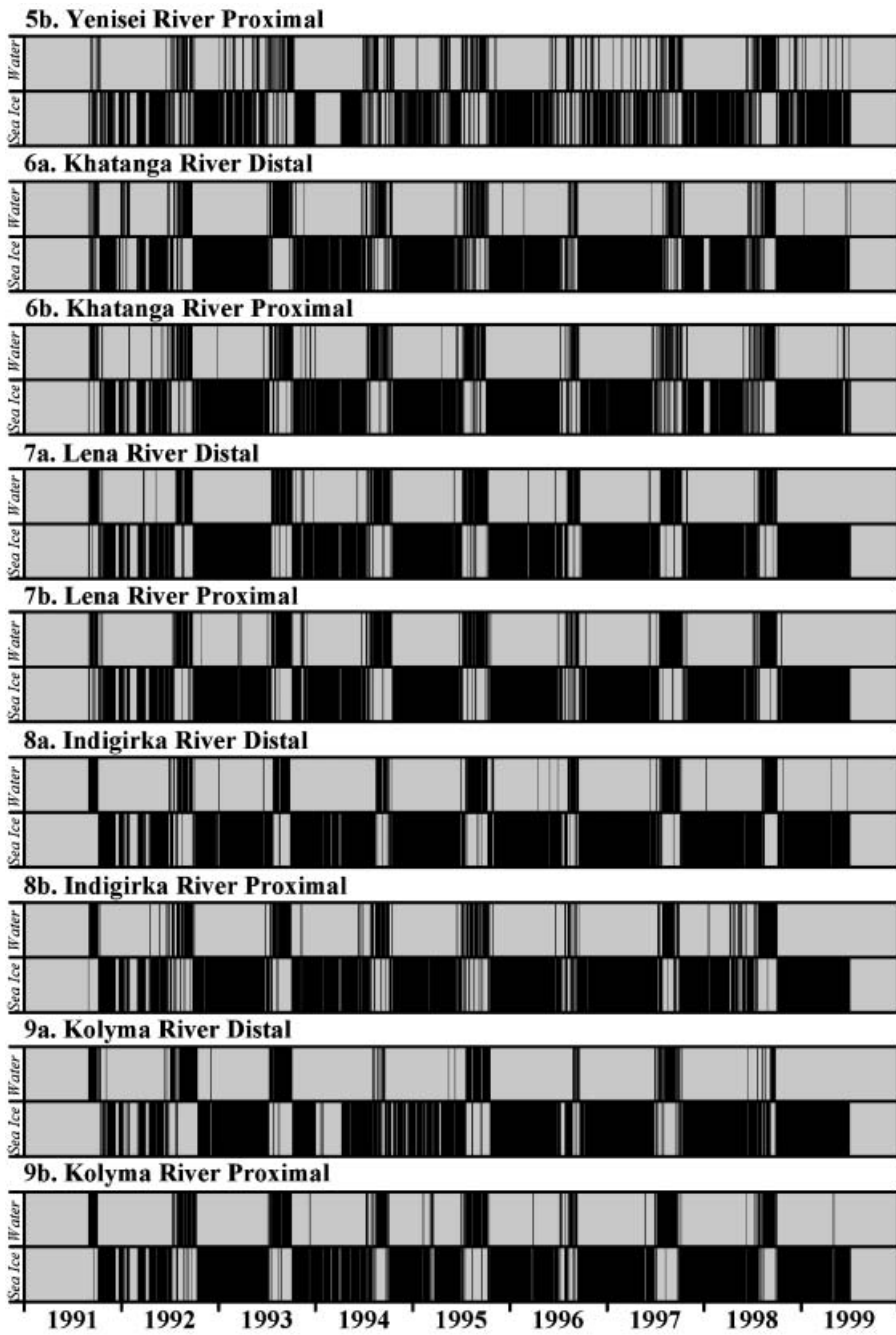


Figure 7. (Continued).

requiring that four of six consecutive flags be water or sea ice ensures that this is a real and persisting seasonal transition. Figure 8(a) presents 1991–1999 averages of the timing of sea ice decay and formation of coastal FYI for all 18 sites.

### 3.2. Regional patterns in melt onset, sea ice formation and decay

Although all of the coastal ice in the present study is considered FYI, radar backscatter signatures of melt onset at western sites (1–4) are similar to those of perennial multi-year sea ice (MYI). In MYI studies, melt onset is detected as a sudden decrease in backscatter (e.g. Winebrenner *et al.* 1994, Yueh and Kwok 1998, Long and Drinkwater 1999, Forster *et al.* 2001). Radar studies observing both MYI and FYI note that the pre-melt backscatter for FYI is considerably lower than MYI (e.g. Barber *et al.* 1992, Wohl 1995, Long and Drinkwater 1999, Forster *et al.*

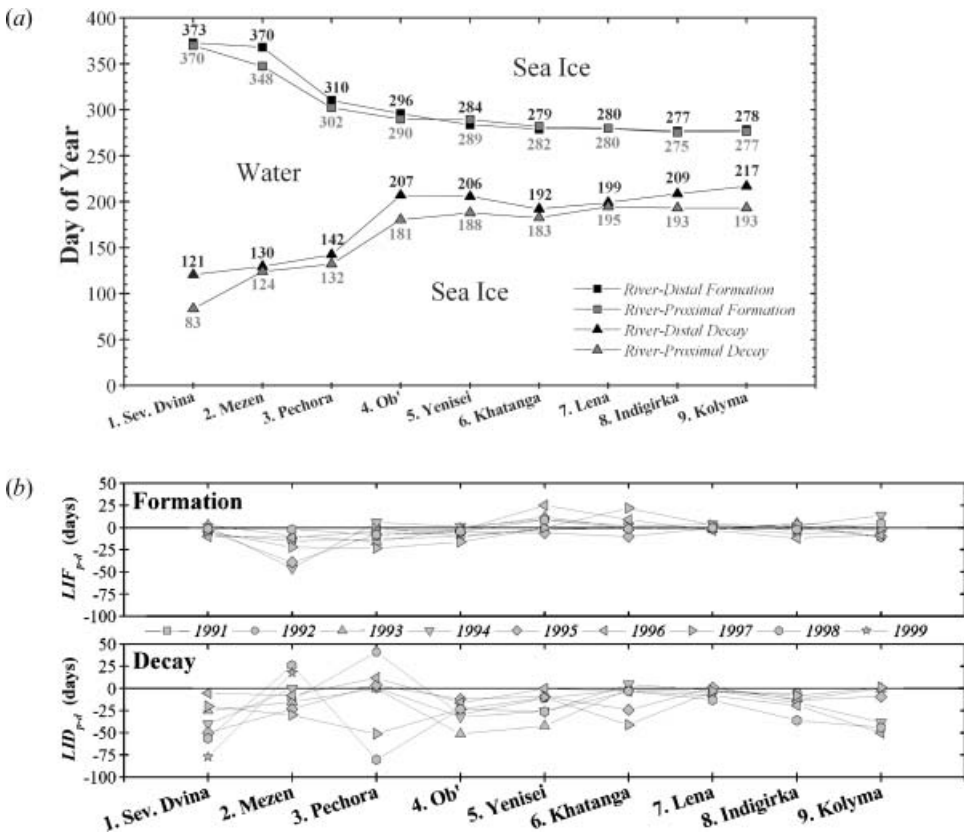


Figure 8. (a) Averaged (1991–1999) dates of sea ice formation and decay for river-distal and river-proximal sites (individual dates are presented in table 1). Ice cover persists longer at sites 4–9 than sites 1–3. With minor exceptions, both sea ice formation and decay occur earlier at proximal sites than distal sites. (b) Inter-annual variability of proximal–distal event timing for each site. Negative  $LIF_{p-d}$  and  $LID_{p-d}$  values indicate earlier sea ice formation and decay at proximal sites. River influence is greater on ice decay than ice formation.  $LID_{p-d}$  values also show more inter-annual variability than  $LIF_{p-d}$  values.

2001), with the onset of snow melt on MYI indicated by decreasing backscatter and on FYI by increasing backscatter (Forster *et al.* 2001).

At sites 5–9, melt onset is detected as a sudden increase in  $\sigma_{40}^0$  (characteristic of FYI). At sites 1–4, however, melt onset is manifested as a decrease in backscatter (characteristic of MYI). Using passive microwave data, similar phenomena were also noted by Anderson (1987), who observed FYI to exhibit sometimes the same melt signature as MYI regions. Although melt-related backscatter decreases are seen for sites 1–3, high backscatter variability makes extraction of melt onset dates problematic. Similar difficulties in detecting melt onset over FYI were encountered by Forster *et al.* (2001). In this study, dates of melt onset could be determined for sites 4–9 only (figure 6, table 1), owing to fluctuating backscatter values and unclear transitions between frozen and thawed states for sites in the Barents Sea. Dates of melt onset at central sites (4–6) display more inter-annual variability than eastern sites (7–9). Earliest dates of melt onset are found at sites 4 and 5 (average day-of-year 130 and 139, respectively), whereas the latest dates are found at site 6 (average day-of-year 160).

Although melt-related backscatter increases for western sites but decreases for eastern sites, backscatter at all sites converges toward similar  $\sigma_{40}^0$  values. Therefore, whether backscatter increases or decreases is determined largely by contrast with pre-melt backscatter levels. Average February backscatter values at western sites (1–3) are  $-15.5$  dB and at eastern sites (7–9) are  $-19.2$  dB. Winter backscatter maps of the area (figure 5(a)) also show relatively high  $\sigma_{40}^0$  values on FYI in western Eurasian seas and MYI farther north ( $-12$  to  $-14$  dB) and relatively low values on FYI in central and eastern Eurasian seas ( $-18$  to  $-20$  dB). Backscatter values of all ice types, however, converge towards an average value of  $\sim -17$  dB at melt onset (figure 5(a), June). These backscatter changes are robust: sites that always increase in backscatter average a change of  $+1.7$  dB; sites that always decrease in backscatter average a change of  $-6.4$  dB.

Figure 7 shows that western sites experience maximum variability in ice cover. Significant differences in the length of open water seasons exist between western and eastern sites as well (figure 5(b), figure 8(a), table 1). On average, ice at western sites (1–3) decays in May, while ice at eastern sites (7–9) does not decay until late July. The average date of ice formation is in early October for eastern sites, but not until December at western sites. The average length of ice cover per year is 144 days at western sites (1–3), 272 days at central sites (4–6) and 289 days at eastern sites (7–9). Thus, western sites experience open water an average of 145 days longer per year than eastern sites.

### 3.3. Effects of rivers on melt onset, sea ice formation and decay

Melt onset is a meteorological, not hydrological event. Therefore, it is not surprising that differences in melt onset dates are minimal between river-distal and river-proximal sites (figure 6, table 1). The largest divergences occur where proximal sites are lower in latitude than distal sites. The Ob' and Yenisei proximal sites (4b and 5b) melt an average 11 and 16 days earlier than their associated distal sites, probably owing to insolation differences (4b and 5b are at higher latitudes). In contrast, small divergences (1–5 days) occur at the Indigirka (site 8) and Kolyma (site 9) rivers, owing to minimal insolation differences. As noted in §3.2., despite

Table 1. Dates of melt onset, sea ice decay and sea ice formation extracted from ERS scatterometer time-series for all 18 sites, 1991–1999. Dates of decay and formation derived from SSM/I passive microwave data are also shown.

	(a) River distal					(b) River proximal				
	ERS Scatterometry			SSM/I Passive Microwave		ERS Scatterometry			SSM/I Passive Microwave	
	Melt Onset	Decay	Formation	Decay	Formation	Melt Onset	Decay	Formation	Decay	Formation
<b>1. Sev. Dvina</b>										
1991	†	†	†	*	*	†	†	†	*	377
1992	*	107	384	114	388	*	†	377	102	387
1993	*	122	361	119	351	*	97	364	115	353
1994	*	143	389	124	388	*	103	390	93	396
1995	*	96	361	107	364	*	46	357	47	357
1996	*	93	391	104	394	*	88	381	87	372
1997	*	146	364	141	364	*	126	360	123	358
1998	*	139	361	138	365	*	83	360	84	362
1999	*	118	*	127	*	*	41	*	81	*
<i>Average ± 1σ</i>	*	<i>120.5 ± 20.9</i>	<i>373 ± 14.2</i>	<i>121.8 ± 13.5</i>	<i>377.3 ± 16.3</i>	*	<i>83.4 ± 30.6</i>	<i>369.9 ± 12.7</i>	<i>91.5 ± 23.4</i>	<i>370.3 ± 15.5</i>
<b>2. Mezen</b>										
1991	†	†	†	*	*	†	†	347	*	339
1992	*	120	377	115	376	*	107	362	114	363
1993	*	142	340	135	351	*	127	331	122	330
1994	*	130	390	131	389	*	130	344	124	332
1995	*	109	391	104	355	*	86	352	83	351
1996	*	133	368	132	370	*	125	357	128	358
1997	*	154	356	137	349	*	124	334	133	333
1998	*	127	355	155	353	*	153	353	146	350
1999	*	123	*	123	*	*	141	*	141	*
<i>Average ± 1σ</i>	*	<i>129.8 ± 13.8</i>	<i>368.1 ± 19.1</i>	<i>129 ± 15.3</i>	<i>364.8 ± 15.3</i>	*	<i>124.1 ± 20.4</i>	<i>347.5 ± 10.8</i>	<i>123.9 ± 19.5</i>	<i>344.5 ± 12.7</i>

Table 1. (Continued)

	(a) River distal					(b) River proximal				
	ERS Scatterometry			SSM/I Passive Microwave		ERS Scatterometry			SSM/I Passive Microwave	
	Melt Onset	Decay	Formation	Decay	Formation	Melt Onset	Decay	Formation	Decay	Formation
<b>3. Pechora</b>										
1991	†	†	323	*	326	†	†	323	*	325
1992	*	131	297	130	295	*	172	284	159	285
1993	*	160	297	156	313	*	160	281	158	296
1994	*	164	311	164	308	*	165	317	168	304
1995	*	79	300	84	312	*	83	292	142	302
1996	*	148	345	154	348	*	160	341	165	346
1997	*	152	315	157	313	*	101	292	172	303
1998	*	163	295	183	296	*	83	287	168	289
1999	*	*	*	*	*	*	*	*	*	*
<i>Average ± 1σ</i>	*	<i>142.4 ± 30.2</i>	<i>310.4 ± 17.2</i>	<i>146.9 ± 31.8</i>	<i>313.9 ± 17</i>	*	<i>132 ± 40.9</i>	<i>302.1 ± 22</i>	<i>161.7 ± 10</i>	<i>306.3 ± 20.1</i>
<b>4. Ob'</b>										
1991	†	†	301	*	299	†	†	292	*	309
1992	133	214	292	206	285	127	185	282	180	282
1993	146	230	290	187	296	146	179	289	158	312
1994	151	215	298	194	302	119	183	299	181	314
1995	108	200	299	194	299	96	188	294	156	315
1996	150	192	301	199	300	128	176	298	173	344
1997	109	199	304	197	305	108	176	288	165	315
1998	145	200	282	201	285	128	177	278	173	285
1999	140	*	*	*	*	141	*	*	*	*
<i>Average ± 1σ</i>	<i>135.3 ± 17.5</i>	<i>207.1 ± 13.1</i>	<i>295.9 ± 7.3</i>	<i>196.9 ± 6</i>	<i>296.4 ± 7.5</i>	<i>124.1 ± 16.4</i>	<i>180.6 ± 4.8</i>	<i>290 ± 7.3</i>	<i>169.4 ± 10</i>	<i>309.5 ± 19.4</i>

Controls on Eurasian coastal sea ice from ERS scatterometry

Table 1. (Continued)

	(a) River distal					(b) River proximal				
	ERS Scatterometry			SSM/I Passive Microwave		ERS Scatterometry			SSM/I Passive Microwave	
	Melt Onset	Decay	Formation	Decay	Formation	Melt Onset	Decay	Formation	Decay	Formation
<b>5. Yenisei</b>										
1991	†	†	290	*	294	†	†	288	*	294
1992	138	209	275	202	278	128	198	274	188	279
1993	166	218	276	184	288	*	176	288	177	287
1994	162	203	289	192	297	*	177	298	171	297
1995	114	191	288	186	290	143	182	282	179	290
1996	170	212	290	197	296	145	212	315	190	296
1997	116	193	286	192	292	113	183	286	182	292
1998	171	214	275	198	276	146	188	284	186	283
1999	144	*	*	*	*	113	*	*	*	*
<i>Average ± 1σ</i>	<i>147.6 ± 23.4</i>	<i>205.7 ± 10.5</i>	<i>283.6 ± 7</i>	<i>193 ± 6.5</i>	<i>288.9 ± 7.9</i>	<i>131.3 ± 15.6</i>	<i>188 ± 12.9</i>	<i>289.4 ± 12.3</i>	<i>181.9 ± 6.7</i>	<i>289.8 ± 6.4</i>
<b>6. Khatanga</b>										
1991	†	†	286	*	283	†	†	286	*	281
1992	170	174	271	203	273	182	173	270	195	272
1993	149	190	282	197	284	150	190	282	190	282
1994	150	187	290	203	292	151	192	292	194	292
1995	155	190	288	199	288	160	166	278	160	280
1996	182	224	259	218	260	185	221	268	202	267
1997	153	210	284	206	286	*	169	306	196	284
1998	154	170	272	204	274	165	167	271	192	274
1999	144	*	*	*	*	144	*	*	*	*
<i>Average ± 1σ</i>	<i>157.1 ± 12.6</i>	<i>192.1 ± 19.1</i>	<i>279 ± 10.7</i>	<i>204.3 ± 6.8</i>	<i>280 ± 10.4</i>	<i>162.4 ± 16</i>	<i>182.6 ± 20.1</i>	<i>281.6 ± 12.9</i>	<i>189.9 ± 13.7</i>	<i>279 ± 7.8</i>

Table 1. (Continued)

	(a) River distal					(b) River proximal				
	ERS Scatterometry			SSM/I Passive Microwave		ERS Scatterometry			SSM/I Passive Microwave	
	Melt Onset	Decay	Formation	Decay	Formation	Melt Onset	Decay	Formation	Decay	Formation
<b>7. Lena</b>										
1991	†	†	283	*	284	†	†	281	*	283
1992	142	199	272	199	273	151	195	272	198	272
1993	140	198	280	197	282	145	198	278	194	282
1994	140	191	286	191	290	149	189	290	195	290
1995	149	186	287	182	288	149	187	287	180	288
1996	138	217	268	213	268	164	209	265	212	266
1997	113	199	285	196	288	114	196	288	195	290
1998	149	203	278	198	277	159	190	278	197	280
1999	140	*	*	*	*	159	*	*	*	*
<i>Average ± 1σ</i>	<i>138.9 ± 11.3</i>	<i>199 ± 9.8</i>	<i>279.9 ± 6.9</i>	<i>196.6 ± 9.3</i>	<i>281.3 ± 7.9</i>	<i>148.8 ± 15.4</i>	<i>194.9 ± 7.4</i>	<i>279.9 ± 8.5</i>	<i>195.9 ± 9.3</i>	<i>281.4 ± 8.6</i>
<b>8. Indigirka</b>										
1991	†	†	281	*	285	†	†	282	*	283
1992	144	194	279	196	281	144	189	272	200	279
1993	143	204	272	199	281	143	192	277	192	278
1994	157	226	278	215	278	157	210	280	204	280
1995	156	198	285	203	291	158	185	288	203	289
1996	141	216	263	221	264	150	197	251	237	259
1997	152	198	277	203	280	147	190	275	199	275
1998	158	225	280	204	280	155	189	278	202	280
1999	156	*	*	*	*	159	*	*	*	*
<i>Average ± 1σ</i>	<i>150.9 ± 7.1</i>	<i>208.7 ± 13.5</i>	<i>276.9 ± 6.7</i>	<i>205.9 ± 8.9</i>	<i>280 ± 7.6</i>	<i>151.6 ± 6.5</i>	<i>193.1 ± 8.3</i>	<i>275.4 ± 11</i>	<i>205.3 ± 14.5</i>	<i>277.9 ± 8.7</i>

Controls on Eurasian coastal sea ice from ERS scatterometry

Table 1. (Continued)

	(a) River distal					(b) River proximal				
	ERS Scatterometry			SSM/I Passive Microwave		ERS Scatterometry			SSM/I Passive Microwave	
	Melt Onset	Decay	Formation	Decay	Formation	Melt Onset	Decay	Formation	Decay	Formation
<b>9. Kolyma</b>										
1991	†	†	290	*	290	†	†	279	*	284
1992	142	†	290	183	295	139	191	287	191	284
1993	142	189	280	186	284	141	189	279	185	279
1994	155	249	264	219	278	152	211	278	203	279
1995	141	200	295	195	297	141	191	285	185	292
1996	138	236	266	228	267	135	186	258	207	265
1997	152	178	270	183	285	146	179	269	180	279
1998	159	249	272	218	284	152	205	277	204	282
1999	176	*	*	*	*	162	*	*	*	*
<i>Average ± 1σ</i>	<i>150.6 ± 12.7</i>	<i>216.8 ± 31.6</i>	<i>278.4 ± 12.1</i>	<i>201.7 ± 19.4</i>	<i>285 ± 9.6</i>	<i>146 ± 8.8</i>	<i>193.1 ± 11.1</i>	<i>276.5 ± 9.2</i>	<i>193.6 ± 10.9</i>	<i>280.5 ± 7.6</i>

\*Not determined

†Data unavailable

strong winter contrasts in backscatter over FYI and MYI, melt onset (June) yields uniform returns converging towards  $\sim -17$  dB (figure 9(a)).

Sea ice cover is typically variable at sites near river mouths (figure 7). Dates of sea ice formation and decay also have a distinct dependence on river proximity. The extent of this river-proximity dependence for local ice formation ( $LIF_{p-d}$ ) and local ice decay ( $LID_{p-d}$ ) is calculated by subtracting scatterometer-derived dates of events at distal sites from those at proximal sites. Therefore, negative values indicate earlier sea ice formation (for  $LIF_{p-d}$ ) and decay (for  $LID_{p-d}$ ) at proximal sites. Figure 8(b) shows the inter-annual variability of both  $LIF_{p-d}$  and  $LID_{p-d}$ . Less inter-annual variability is found in  $LIF_{p-d}$  and temporal averages (1991–1999) for each site range from  $-22$  days (site 2) to  $+5$  days (site 5) (figure 8(a)). Averaged across all sites, sea ice formation takes place 3.7 days earlier at proximal sites than distal sites (figure 8(a), table 1). Greater inter-annual variability is found in  $LID_{p-d}$  and temporal averages (1991–1999) for each site range from  $-38$  days (site 1) to  $-4$  days (site 7) (figure 8(b)). Averaged across all sites, sea ice decays 16.8 days earlier at proximal sites than distal sites (figure 8(a), table 1). This lag in decay is spatially apparent in maps of  $B$  in the Kolyma River region (figure 9(b), August). It must also be mentioned that the Lena River distal site (7a) and the Indigirka River distal site (8a) are situated in proximity of the Bykov channel of the Lena Delta and the Alazeya River, respectively. This may cause these sites to be affected also by river influx, although probably not to as great an extent as their associated river-proximal sites.

Figure 10 compares scatterometer-derived dates of sea ice decay at river-proximal sites with timing of the annual spring flood. Discharge records from the Sev. Dvina, Mezen and Pechora rivers are available until 1993, and from the Ob', Yenisei, Lena, Indigirka and Kolyma rivers until 1994. Discharge records from the Khatanga River do not temporally coincide with available scatterometer data. Westernmost sites (1 and 2) experience decay  $\sim 4$  weeks earlier than the spring flood. Central sites (4 and 5) experience decay  $\sim 3$  weeks after the spring flood. Easternmost sites (8 and 9) experience decay nearly 6 weeks after the spring flood. In general, the time lag between initial flooding and the disappearance of coastal FYI increases from west to east along the Arctic Eurasian coast.

#### 4. Validation of results using meteorological and SSM/I passive microwave data

Meteorological station air temperature data show good agreement with scatterometer observations of melt onset and sea ice formation (figure 11). For each year, melt onset is chosen as the first day that air temperatures exceed  $0^\circ\text{C}$ . Minimum day-of-year for sea ice formation is chosen as the first negative degree-day. Tiksi station data are selected for validation owing to Tiksi's coastal location and short distance to site 7a (38 km) (figure 1). Melt onset dates at site 7a average 4.1 days later than those identified in meteorological station data, although a larger difference is seen in 1994 (19 days). Scatterometer-derived sea ice formation dates at site 7a average 13.1 days later than those chosen from meteorological station data. This lag is not surprising, since it is unlikely that uniform sea ice cover is formed on the first negative degree-day. In addition to air temperature, additional factors such as salinity, wind speed, dew point and incoming solar radiation are also important in sea ice formation (Danard *et al.* 1983).

SSM/I sea ice concentrations are also used to validate scatterometer

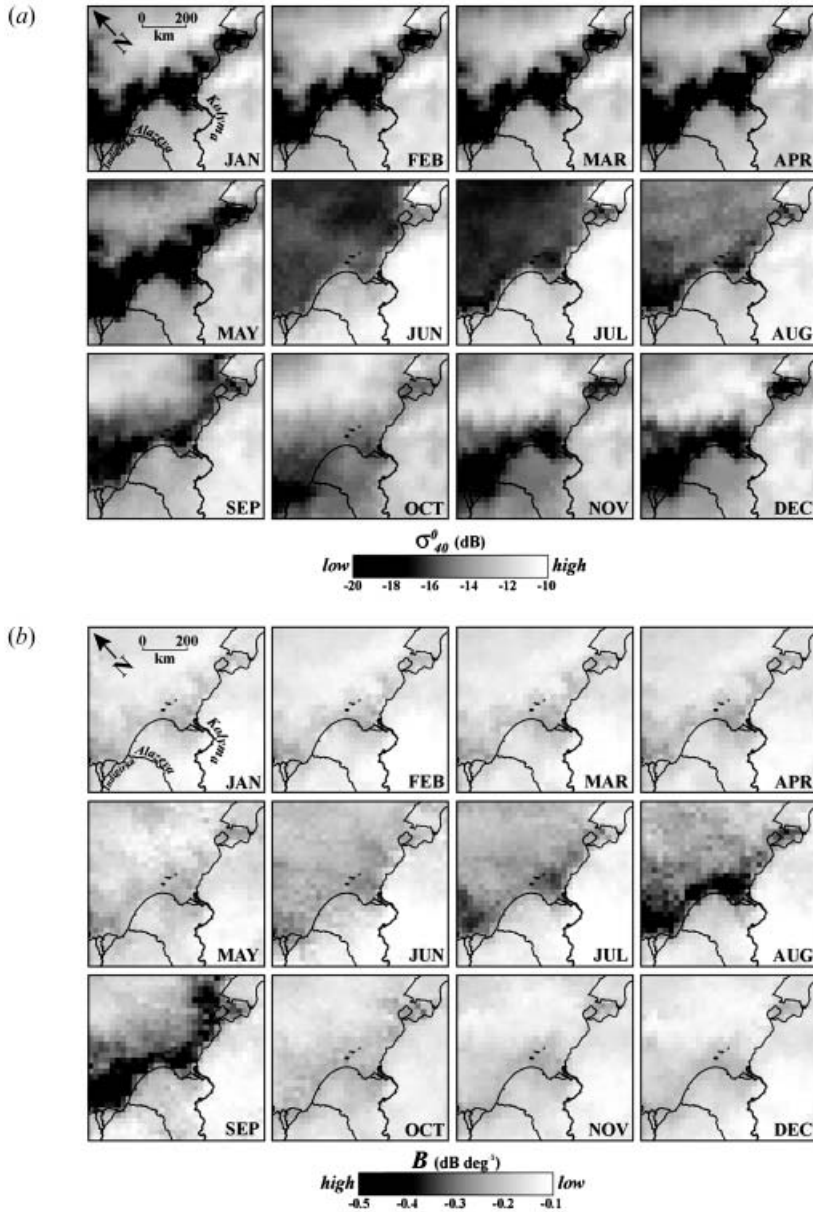


Figure 9. (a) Monthly averaged ERS scatterometer  $\sigma_{40}^0$  maps of the Kolyma River and surrounding coastal area. Despite strong winter contrasts in backscatter over FYI (along the coast) and MYI (farther north), melt onset yields uniform backscatter returns in June. (b) Monthly averaged ERS scatterometer  $B$  maps of the Kolyma River and surrounding coastal area. Ice decay, indicated by an increase in  $B$  magnitude, initiates near river mouths in July and propagates along the coastline in August and September. Ice formation, indicated by a decrease in  $B$  magnitude, occurs in October.

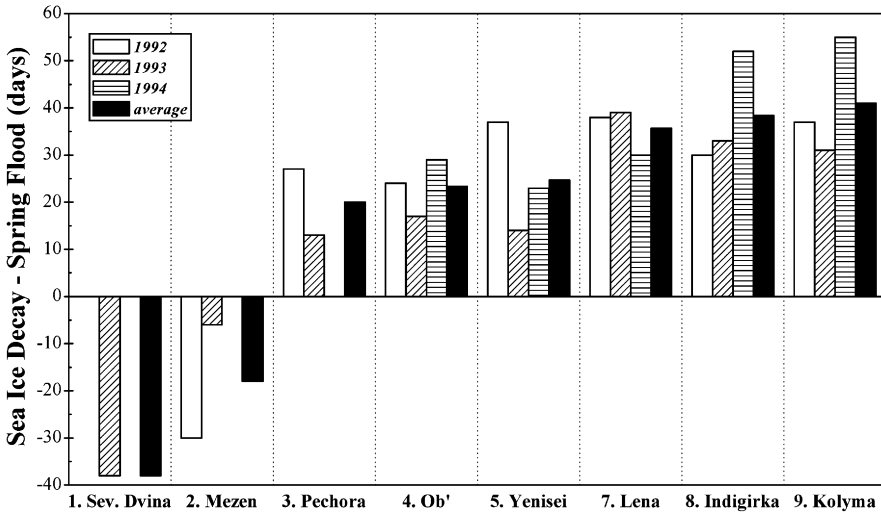


Figure 10. Differences between dates of scatterometer-derived sea ice decay (at river-proximal sites) and the spring flood of associated rivers. Sea ice decay precedes the arrival of the spring flood at the Sev. Dvina and Mezen rivers. River flooding precedes sea ice decay at the Pechora, Ob', Yenisei, Lena, Indigirka and Kolyma rivers, with lags increasing eastward. Discharge data were not available for the Khatanga River.

observations of sea ice decay and formation (table 1). For date extraction purposes, sea ice concentrations are first normalized using the same step (4) applied to the scatterometer data (§2.3.), yielding positive values for sea ice and negative values for open water. Initial ice/water classifications from scatterometer  $B^*$  data alone are in

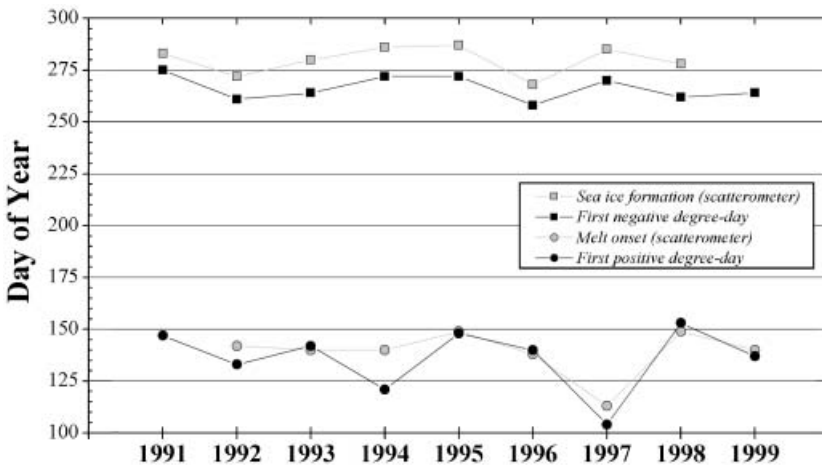


Figure 11. Comparison of melt onset and sea ice formation dates derived from ERS scatterometer data (site 7a) and meteorological station air temperature data at Tiksi. Scatterometer-derived melt onset agrees well with the first positive degree-day of each year. Scatterometer-derived dates of ice formation are consistently ~2 weeks later than the first negative degree-day of each year.

85% agreement with those from SSM/I (figure 12(a)). Higher ambiguity in quadrant IIIa is likely caused by wind-roughened waters, which yield  $B^*$  values similar to those of ice and snow. Addition of an anisotropy ( $\sigma_{f-a}^0$ ) criterion (§3.1.) slightly improves agreement to 87.5% (figure 12(b)).

Figure 13 suggests that ERS scatterometer data and SSM/I sea ice concentrations detect FYI decay and formation with close agreement. In fact, correlation of all decay and formation dates between the two datasets results in an  $R^2$  value of 0.97. Closer examination of the less erratic data at sites 4–9 shows that ERS scatterometers detect decay  $\sim 2$  days later and formation  $\sim 4$  days earlier than the SSM/I instrument. This difference is likely evident because scatterometer data are sensitive to the surface scattering mechanism and anisotropy magnitude, whereas SSM/I sea ice concentrations are highly dependent on surface temperature and the emissivity of the medium (Choudhury 1989). Scatterometer data and SSM/I sea ice concentrations therefore yield similar sea ice decay and formation dates, yet for different physical reasons.

## 5. Discussion

### 5.1. Regional variability

A strong regional pattern is seen in the temporal variability of both melt onset and FYI cover. Maximum variability is seen in the Barents and Kara seas, with

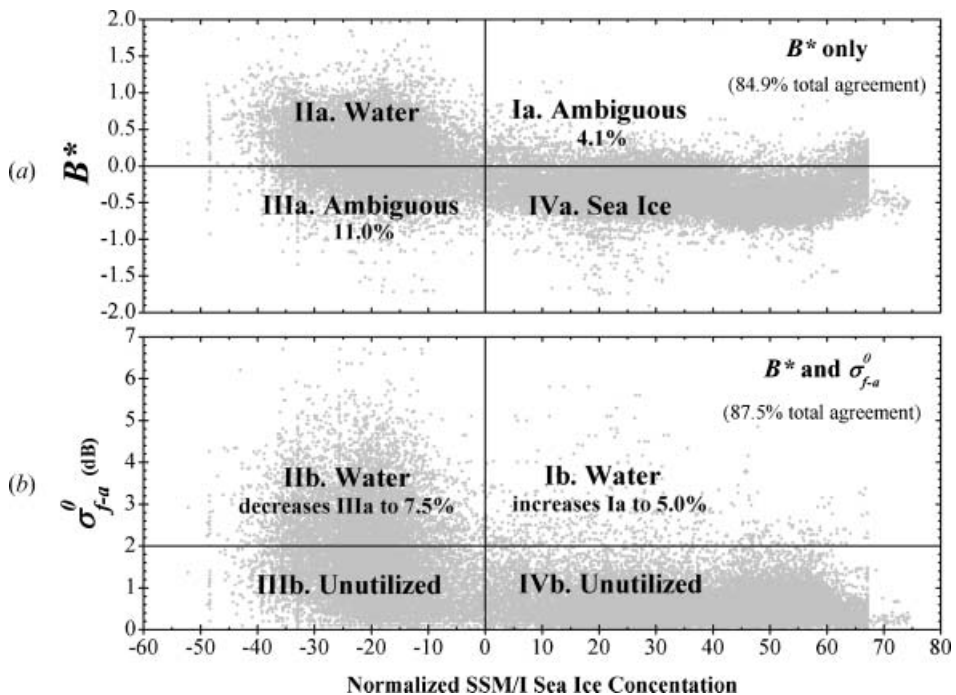


Figure 12. Comparison of scatterometer data and normalized SSM/I sea ice concentration for all 18 sites, 1991–1999. (a) Quadrants IIa and IVa show 85% agreement between scatterometer  $B^*$  and SSM/I. Ambiguous results arise when the two datasets give conflicting flags for sea ice and open water (quadrants Ia and IIIa). (b) With the addition of azimuthal modulation criterion ( $\sigma_{f-a}^0$ ), the total agreement between datasets increases to 87.5%.

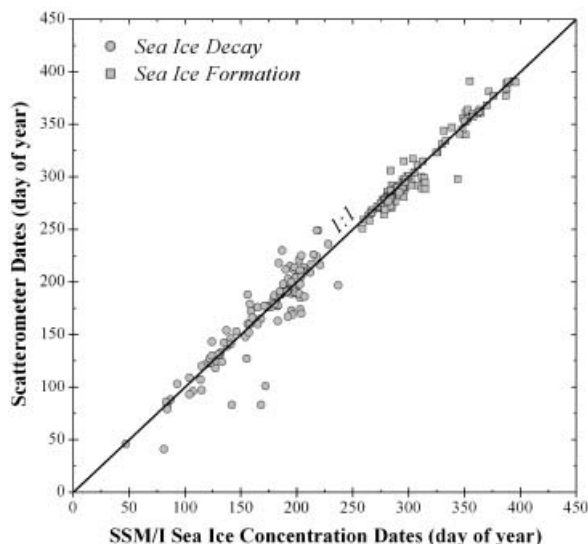


Figure 13. Comparison of ERS scatterometer and SSM/I-derived sea ice decay and formation dates. The line represents 1:1 correlation. For sites 4–9, scatterometry detects decay  $\sim 2$  days later and formation  $\sim 4$  days earlier than passive microwave radiometry.

decreasing variability eastward (figures 6 and 7). In winter, this pattern likely reflects regional contrasts in air temperature and snowfall. West–east contrasts are found in air temperatures (Tao *et al.* 1996), with western Siberia more closely resembling the North Atlantic region. Western sites experience winter air temperatures that often rise above freezing (figure 4(c)(iv)), unlike sites farther east (figure 4(a)(iv), (b)(iv)). The western Eurasian coastline also receives more insolation than eastern Eurasia, owing to its lower latitude. Frequent shifts from below to above freezing air temperatures promote greater variability in backscatter signatures owing to brief snow melt events. A pronounced North Atlantic cyclone track also promotes frequent snowfall events in the region, with dense cyclonic activity extending into the Barents and Kara seas (Murray and Simmonds 1995, Serreze *et al.* 1995b). Western Eurasian seas experience significantly greater snowfall than eastern Eurasian seas, where snowstorms occur about 100–120 days per year in the Barents and Kara seas but only 60–80 days per year in the Laptev and East Siberian seas (Proshutinsky *et al.* 1998). We speculate that the high variability for western sites seen in backscatter (figure 4(c)(i)) and sea ice (figure 7) results from a combination of frequent surface melting events (promoting surface scattering and increased  $B$  values) and snowfall events (promoting volume scattering and decreased  $B$  values).

A strong west–east contrast is also seen in the scatterometer-derived length of open water seasons. The average length of open water per year at western sites (1–3) is 145 days longer than at eastern sites (7–9). This observation is consistent with the longer duration of above freezing temperatures at western sites (figure 4(c)(iv)) as compared with eastern sites (figure 4(a)(iv), (b)(iv)). High-salinity (34–35‰) waters in the Barents Sea (Aagaard and Carmack 1989), driven by the warm, saline North Atlantic and Norwegian Currents (Parkinson *et al.* 1987), also

contribute to decreased ice cover. The elongate island of Novaya Zemlya separates the Barents and Kara seas (figure 1), acting as a barrier to the eastward flow of these waters. As a result, Novaya Zemlya often marks a sharp contrast in ice cover (figure 5(b)). Freshwater influx from large rivers further decreases salinity (26–30‰) eastward in the Laptev and East Siberian seas (Parkinson *et al.* 1987). Greater snowfall in the west may also contribute to our observation of shorter-lived sea ice there. Snow has significant effects on the thermodynamics, formation and ablation of sea ice owing to its relatively low thermal conductivity (Brown and Cote 1992), the presence of which may cause sea ice in the west to be more transient. We speculate that our observation of shorter-lived sea ice in the west (figure 8(a)) is caused by a combination of the insulating effects of snow, a shorter season of below-freezing air temperatures, and high-salinity waters.

Greater snowfall in the west may also contribute to the  $\sim 3.7$  dB higher winter backscatter values we observe there. Onstott (1992) found FYI with up to 8 cm of snow cover to have backscatter coefficients 1–5 dB higher than snow-free FYI. The complex permittivity at the snow–ice interface is considerably higher than that of a bare ice surface, owing to a warmer interface produced by the insulating effects of snow. This warmer interface increases the brine volume in the basal layer of the snow, creating a ‘dielectrically rough’ surface (Barber *et al.* 1998), yielding higher backscatter values. Regardless of mechanism, we observe regional contrasts in winter backscatter values over FYI. These contrasts are consistent with pre-melt winter backscatter differences seen between MYI and FYI in other studies (Barber *et al.* 1992, Wohl 1995, Forster *et al.* 2001). It is this contrast that leads to the often confusing observation that melt onset causes a backscatter increase in some locations, but a decrease in others (e.g. Forster *et al.* 2001). Our observations show that, in fact, all melt signatures converge to  $\sim -17$  dB, hence whether backscatter increases or decreases depends only on pre-melt backscatter levels.

### 5.2. Local variability

Observed local contrasts in sea ice variability (figure 8(b)) are likely caused by freshwater influx from nearby rivers. Decreased salinity near river mouths may explain why ice forms an average 3.7 days earlier at proximal sites than distal sites (figure 8(a)). Proximal sites freeze earlier at all sites except 5 and 6, where differences in the timing of formation are still minimal. Ice formation takes place earlier even at proximal sites that are significantly lower in latitude than their distal counterparts (sites 1–4). Every proximal site averages a sea ice decay date earlier than its associated distal site, including 7–9, where proximal sites are at the same or higher latitudes. Averaged for all sites, sea ice near river mouths decays 16.8 days earlier than sites farther away (figure 8(a)). This is in close agreement with the 14-day difference in sea ice regression found by Dean *et al.* (1994) and Searcy *et al.* (1996) near the Mackenzie River. For the Pechora, Ob', Yenisei, Lena, Indigirka and Kolyma rivers, the annual spring flood precedes ice decay by an average of 20–41 days (figure 10). This observation suggests that thermal decay and/or reduced ice albedo from overflowing and sediment deposition may be significant in these regions. A thermodynamic model of sea ice (Bareiss *et al.* 1999) shows that following river overflowing, land-fast ice disintegrates in approximately 28 days. This lag is consistent with our observations in central and eastern Eurasian seas. However, lags between river flooding and ice disappearance increase significantly

from west to east (figure 10). Ice decay at western sites actually precedes river flooding, indicating no significant hydrological influence. Central sites experience a shorter lag than eastern sites, suggesting that the Ob', Yenisei and Lena rivers have a stronger influence on sea ice decay, probably owing to their greater discharge. Rivers exert less influence in eastern Siberia, probably owing to smaller discharges and greater sea ice thickness and continuity.

## 6. Conclusions

Time-series of ERS scatterometer backscatter and incident angle relationships are used to identify patterns of sea ice formation, melt onset and decay along coastal Eurasia. We speculate that strong regional contrasts in ice characteristics are due to North Atlantic modulation of air temperature, salinity and cyclone density. These factors cause coastal ice cover in western Eurasian seas to be temporally variable and shorter-lived than ice in eastern Eurasian seas. Rivers also exert a local effect on ice cover, causing earlier formation and decay near river mouths. These effects are attributed to thermal input, ice overflowing and decreased salinity from river discharge. River influence on the local decay of sea ice is potentially strong in central and eastern Eurasia but absent in western Eurasia. This study presents a first application of ERS scatterometer data to determine the timing of FYI formation and breakup. Nearly ten years of global scatterometer data were collected by the ERS satellites, a large portion of which still remains untapped. The methodology presented here has potential use for these data in a wide variety of FYI studies.

## Acknowledgments

Funding for this research was provided by the National Science Foundation, Office of Polar Programs, Arctic Systems Science Program (project OPP-9708997). Support to D. E. Alsdorf was also provided by NASA (project NAG5-9055). ERS scatterometer data were provided by the Centre ERS d'Archivage et de Traitement (CERSAT), the French Processing and Archiving Facility (F-PAF) (Brest, France). Additional data were provided by the National Snow and Ice Data Center (Boulder, Colorado, USA), the National Climatic Data Center (Asheville, North Carolina, USA), and the Global Runoff Data Centre in the Federal Institute of Hydrology (Koblenz, Germany).

## References

- AAGAARD, K., and CARMACK, E. C., 1989, The role of sea ice and other fresh water in the Arctic circulation. *Journal of Geophysical Research*, **94**, 14485–14498.
- ANDERSON, M. R., 1987, The onset of spring melt in first-year ice regions of the Arctic as determined from scanning multichannel microwave radiometer data for 1979 and 1980. *Journal of Geophysical Research*, **92**, 13153–13163.
- BARBER, D. G., LEDREW, E. F., FLETT, D. G., SHOKR, M., and FALKINGHAM, J., 1992, Seasonal and diurnal variations in SAR signatures of landfast sea ice. *IEEE Transactions on Geoscience and Remote Sensing*, **30**, 638–642.
- BARBER, D. G., FUNG, A. K., GRENFELL, T. C., NGHIEM, S. V., ONSTOTT, R. G., LYTLE, V. I., PEROVICH, D. K., and GOW, A. J., 1998, The role of snow on microwave emission and scattering over first-year sea ice. *IEEE Transactions on Geoscience and Remote Sensing*, **36**, 1750–1763.
- BAREISS, J., EICKEN, H., HELBIG, A., and MARTIN, T., 1999, Impact of river discharge and

- regional climatology on the decay of sea ice in the laptev Sea during spring and early summer. *Arctic, Antarctic, and Alpine Research*, **31**, 214–229.
- BARRY, R. G., SERREZE, M. C., and MASLANIK, J. A., 1993, The Arctic sea ice–climate system: observations and modelling. *Reviews of Geophysics*, **31**, 397–422.
- BROWN, R. D., and COTE, P., 1992, Interannual variability of landfast ice thickness in the Canadian High Arctic, 1950–89. *Arctic*, **45**, 273–284.
- CARMACK, E. C., 1990, Large scale physical oceanography of polar seas. In *Polar Oceanography*, edited by W. O. Smith (New York: Academic Press), pp. 171–222.
- CAVALIERI, D. J., GLOERSEN, P., PARKINSON, C. L., COMISO, J. C., and ZWALLY, H. J., 1997, Observed hemispheric asymmetry in global sea ice changes. *Science*, **278**, 1104–1106.
- CAVALIERI, D., PARKINSON, C., GLOERSON, P., and ZWALLY, H. J., 1999, updated 2002, *Sea Ice Concentrations from Nimbus-7 SMMR and DMSP SSM/I Passive Microwave Data* (Boulder, CO, USA: National Snow and Ice Data Center).
- CAVANIÉ, A., 1998, An empirical C-band backscatter melt over arctic sea ice from ERS-1 AMI-wind data. *Proceedings of a Joint ESA–Eumetstat Workshop on Emerging Scatterometer Applications—from Research to Operations, 5–7 October 1998* (Noordwijk, The Netherlands: ESA), pp. 99–106.
- CHOUDHURY, B. J., 1989, Monitoring global land surface using Nimbus-7 37 GHz data: theory and examples. *International Journal of Remote Sensing*, **10**, 1579–1605.
- CLARK, M. P., SERREZE, M. C., and ROBINSON, D. A., 1999, Atmospheric controls on Eurasian snow extent. *International Journal of Climatology*, **19**, 27–40.
- COOK, E. R., D'ARRIGO, R. D., and BRIFFA, K. R., 1998, A reconstruction of the North Atlantic Oscillation using tree-ring chronologies from North America and Europe. *Holocene*, **8**, 9–17.
- DANARD, M., GRAY, M., and LYV, G., 1983, A model for the prediction of initial sea ice formation. *Monthly Weather Review*, **111**, 1634–1645.
- DEAN, K. G., STRINGER, W. J., AHLNÄS, K., SEARCY, C., and WEINGARTNER, T., 1994, The influence of river discharge on the thawing of sea ice, Mackenzie River Delta: albedo and temperature analyses. *Polar Research*, **13**, 83–94.
- DRINKWATER, M. R., and CARSEY, F. D., 1991, Observations of the late-summer to fall transition with the 14.6 GHz SEASAT scatterometer. *Proceedings of the International Geoscience and Remote Sensing Symposium, 3–6 June 1991* (New York: IEEE Publications), pp. 1597–1600.
- DRINKWATER, M. R., and LIU, X., 2000, Seasonal to interannual variability in Antarctic sea-ice surface melt. *IEEE Transactions on Geoscience and Remote Sensing*, **38**, 1827–1842.
- DRINKWATER, M. R., WADHAMS, P., LOW, D., and LIU, X., 1998, Interannual variability in Weddell Sea ice from ERS wind scatterometer. *Proceedings of a Joint ESA–Eumetstat Workshop on Emerging Scatterometer Applications—from Research to Operations, 5–7 October 1998* (Noordwijk, The Netherlands: ESA), pp. 119–123.
- EARLY, D. S., and LONG, D. G., 1997, Azimuthal modulation of C-band scatterometer  $\sigma^0$  over southern ocean sea ice. *IEEE Transactions on Geoscience and Remote Sensing*, **35**, 1201–1209.
- ESA (European Space Agency), 1993, ERS-1 User Handbook, Revision 1. ESA SP-1148, ESA Publications Division, Noordwijk, The Netherlands.
- EZRATY, R., and CAVANIÉ, A., 1999a, Construction and evaluation of 12.5-km grid NSCAT backscatter maps over Arctic sea ice. *IEEE Transactions on Geoscience and Remote Sensing*, **37**, 1685–1697.
- EZRATY, R., and CAVANIÉ, A., 1999b, Intercomparison of the backscatter maps over Arctic sea ice from NSCAT and the ERS scatterometer. *Journal of Geophysical Research*, **104**, 11 471–11 483.
- FORMAN, S. L., and JOHNSON, G. L., 1998, Prospectus for the Russian–American Initiative on Shelf-Land Environments in the Arctic (RAISE). Arctic Research Consortium of the United States (ARCUS), Fairbanks, AK, USA.
- FORSTER, R. R., LONG, D. G., JEZEK, K. C., DROBOT, S. D., and ANDERSON, M. R., 2001, The onset of Arctic sea-ice melt as detected with passive and active remote sensing. *Annals of Glaciology*, **33**, 85–93.

- GOHIN, F., and CAVANIÉ, A., 1994, A first try at identification of sea ice using the three beam scatterometer of ERS-1. *International Journal of Remote Sensing*, **15**, 1221–1228.
- GORDEEV, V. V., MARTIN, J. M., SIDOROV, I. V., and SIDOROVA, M. V., 1996, A reassessment of the Eurasian River input of water, sediment, major elements and nutrients to the Arctic Ocean. *American Journal of Science*, **296**, 664–691.
- GRANDELL, J., JOHANNESSEN, J. A., and HALLIKAINEN, M. T., 1999, Development of a synergetic sea ice retrieval method for the ERS-1 AMI wind scatterometer and SSM/I radiometer. *IEEE Transactions on Geoscience and Remote Sensing*, **37**, 668–679.
- GREBMEIER, J. M., WHITLEDGE, T. E., CODISPOTI, L. A., DUNTON, K. H., WALSH, J. J., WEINGARTNER, T. J., and WHEELER, P. A., 1998, Arctic system science ocean–atmosphere–ice interactions; western Arctic shelf–basin interactions science plan. ARCSS/OAII Report Number 7, Old Dominion University, Norfolk, VA, USA.
- GRIFFIES, S. M., and BRYAN, K., 1997, Predictability of North Atlantic multidecadal climate variability. *Science*, **275**, 181–184.
- HAAS, C., 2001, The seasonal cycle of ERS scatterometer signatures over perennial Antarctic sea ice and associated surface ice properties and processes. *Annals of Glaciology*, **33**, 69–73.
- HÄKKINEN, S., and GEIGER, C. A., 2000, Simulated low-frequency modes of circulation in the Arctic Ocean. *Journal of Geophysical Research*, **105**, 6549–6564.
- HALL, D. K., 1998, Remote sensing of snow and ice using imaging radar. In *Principles and Applications of Imaging Radar (Manual of Remote Sensing, Vol. 2)*, edited by F. M. Henderson and A. J. Lewis (New York: Wiley & Sons), pp. 677–703.
- HALL, M. M., and BRYDEN, H. L., 1982, Direct estimates and mechanisms of ocean heat-transport. *Deep-Sea Research Part A, Oceanographic Research Papers*, **29**, 339–359.
- HALPERT, M. S., and BELL, G. D., 1997, Climate assessment for 1996. *Bulletin of the American Meteorological Society*, **78**, S1–S49.
- HILMER, M., and LEMKE, P., 2000, On the decrease of Arctic sea ice volume. *Geophysical Research Letters*, **27**, 3751–3754.
- HOLT, T., KELLY, P. M., and CHERRY, B. S. G., 1984, Cryospheric impacts of Soviet river diversions. *Annals of Glaciology*, **5**, 61–68.
- HURRELL, J. W., 1995, Decadal trends in the North-Atlantic Oscillation—regional temperatures and precipitation. *Science*, **269**, 676–679.
- HURRELL, J. W., 1996, Influence of variations in extratropical wintertime teleconnections on Northern Hemisphere temperature. *Geophysical Research Letters*, **23**, 665–668.
- HURRELL, J. W., and VANLOON, H., 1997, Decadal variations in climate associated with the north Atlantic oscillation. *Climatic Change*, **36**, 301–326.
- JOHANNESSEN, O. M., SHALINA, E. V., and MILES, M. W., 1999, Satellite evidence for an Arctic sea ice cover in transformation. *Science*, **286**, 1937–1939.
- KEELING, C. D., CHIN, J. F. S., and WHORF, T. P., 1996, Increased activity of northern vegetation inferred from atmospheric CO<sub>2</sub> measurements. *Nature*, **382**, 146–149.
- KENNETT, R. G., and LI, F. K., 1989, Seasat over-land scatterometer data, part I: global overview of the Ku-band backscatter coefficients. *IEEE Transactions on Geoscience and Remote Sensing*, **27**, 592–605.
- KERR, R. A., 1999, A new force in high-latitude climate. *Science*, **284**, 241–242.
- KWOK, R., NGHIEM, S. V., MARTIN, S., WINEBRENNER, D. P., GOW, A. J., PEROVICH, D. P., SWIFT, C. T., BARBER, D. G., GOLDEN, K. M., and KNAPP, E. J., 1998, Laboratory measurements of sea ice: connections to microwave remote sensing. *IEEE Transactions on Geoscience and Remote Sensing*, **36**, 1716–1730.
- LEHMAN, S. J., and KEIGWIN, L. D., 1992, Sudden changes in north-Atlantic circulation during the last deglaciation. *Nature*, **356**, 757–762.
- LEVITUS, S., 1982, Climatological atlas of the world ocean. NOAA Professional Paper, 13, US Department of Commerce, NOAA, Washington, DC, USA.
- LONG, D. G., and DRINKWATER, M. R., 1999, Cryosphere applications of NSCAT data. *IEEE Transactions on Geoscience and Remote Sensing*, **37**, 1671–1684.
- LONG, D. G., HARDIN, P. J., and WHITING, P. T., 1993, Resolution enhancement of spaceborne scatterometer data. *IEEE Transactions on Geoscience and Remote Sensing*, **31**, 700–715.

- MACDONALD, G., FELZER, B., FINNEY, B., and FORMAN, S., 2000a, Holocene lake sediment records of Arctic hydrology. *Journal of Paleolimnology*, **24**, 1–14.
- MACDONALD, G. M., VELICHKO, A. A., KREMENTSKI, C. V., BORISOVA, O. K., GOLEVA, A. A., ANDREEV, A. A., CWYNAR, L. C., RIDING, R. T., FORMAN, S. L., EDWARDS, T. W. D., ARAVENA, R., HAMMARLUND, D., SZEICZ, J. M., and GATTAULIN, V. N., 2000b, Holocene treeline history and climate change across northern Eurasia. *Quaternary Research*, **53**, 302–311.
- MANABE, S., STOUFFER, R. J., SPELLMAN, M. J., and BRYAN, K., 1991, Transient response of a coupled ocean–atmosphere model to gradual changes of atmospheric CO<sub>2</sub>. Part I: Annual mean response. *Journal of Climate*, **4**, 785–818.
- MANAK, D. K., and MYSAK, L. A., 1989, On the relationship between Arctic sea-ice anomalies and fluctuations in northern Canadian air temperature and river discharge. *Atmosphere–Ocean*, **27**, 682–691.
- MASLANIK, J. A., SERREZE, M. C., and BARRY, R. G., 1996, Recent decreases in Arctic summer ice cover and linkages to atmospheric circulation anomalies. *Geophysical Research Letters*, **23**, 1677–1680.
- MATTHEWS, J. B., and STRINGER, W. J., 1984, Spring breakup and flushing of an Arctic lagoon estuary. *Journal of Geophysical Research*, **89**, 2073–2079.
- MURRAY, R. J., and SIMMONDS, I., 1995, Responses of climate and cyclones to reductions in Arctic winter sea ice. *Journal of Geophysical Research*, **100**, 4791–4806.
- ONSTOTT, R. G., 1992, SAR and scatterometer signatures of sea ice. In *Microwave Remote Sensing of Sea Ice*, edited by F. D. Carsey (Washington, DC: American Geophysical Union), pp. 73–104.
- PARKINSON, C. L., COMISO, J. C., ZWALLY, H. J., CAVALIERI, D. J., GLOERSON, P., and CAMPBELL, W. J., 1987, *Arctic Sea Ice, 1973–1976: Satellite Passive-Microwave Observations* (Washington, D.C.: Scientific and Technical Information Branch, National Aeronautics and Space Administration).
- PARKINSON, C. L., CAVALIERI, D. J., GLOERSON, P., ZWALLY, H. J., and COMISO, J. C., 1999, Arctic sea ice extents, areas, and trends, 1978–1996. *Journal of Geophysical Research*, **104**, 20837–20856.
- PENG, S. L., and MYSAK, L. A., 1993, A teleconnection study of interannual sea-surface temperature—fluctuations in the northern North-Atlantic and precipitation and runoff over western Siberia. *Journal of Climate*, **6**, 876–885.
- PERLWITZ, J., and GRAF, H. F., 1995, The statistical connection between tropospheric and stratospheric circulation of the Northern-Hemisphere in winter. *Journal of Climate*, **8**, 2281–2295.
- POLYAKOV, I. V., PROSHUTINSKY, A. Y., and JOHNSON, M. A., 1999, Seasonal cycles in two regimes of Arctic climate. *Journal of Geophysical Research*, **104**, 25761–25788.
- PROSHUTINSKY, A. Y., and JOHNSON, M. A., 1997, Two circulation regimes of the wind-driven Arctic Ocean. *Journal of Geophysical Research*, **102**, 12493–12514.
- PROSHUTINSKY, A. Y., PROSHUTINSKY, T., and WEINGARTNER, T., 1998, 1998 Final Report, INSROP Phase 2 Projects, Natural Conditions and Ice Navigation, Project 2. (Lysaker, Norway: The Fridtjof Nansen Institute).
- PROSHUTINSKY, A. Y., POLYAKOV, I. V., and JOHNSON, M. A., 1999, Climate states and variability of Arctic ice and water dynamics during 1946–1997. *Polar Research*, **18**, 135–142.
- RAMANATHAN, V., 1988, The greenhouse theory of climatic change: a test by an inadvertent global experiment. *Science*, **240**, 293–299.
- REMUND, Q. P., and LONG, D. G., 1999, Sea ice extent mapping using Ku band scatterometer data. *Journal of Geophysical Research*, **104**, 11515–11527.
- REMUND, Q. P., LONG, D. G., and DRINKWATER, M. R., 2000, An iterative approach to Multisensor sea ice classification. *IEEE Transactions on Geoscience and Remote Sensing*, **38**, 1843–1856.
- ROEMMICH, D., and WUNSCH, C., 1985, Two transatlantic sections: meridional circulation and heat-flux in the sub-tropical North-Atlantic Ocean. *Deep-Sea Research Part A, Oceanographic Research Papers*, **32**, 619–664.
- ROGERS, J. C., and MOSLEY-THOMPSON, E., 1995, Atlantic Arctic cyclones and the mild Siberian winters of the 1980s. *Geophysical Research Letters*, **22**, 799–802.

- SEARCY, C., DEAN, K., and STRINGER, W., 1996, A river-coastal sea ice interaction model: Mackenzie River Delta. *Journal of Geophysical Research*, **101**, 8885–8894.
- SERREZE, M. C., MASLANIK, J. A., KEY, J. R., KOKALY, R. F., and ROBINSON, D. A., 1995a, Diagnosis of the record minimum in the Arctic sea ice area during 1990 and associated snow cover extremes. *Geophysical Research Letters*, **22**, 2183–2186.
- SERREZE, M. C., BARRY, R. G., REHDER, M. C., and WALSH, J. E., 1995b, Variability in atmospheric circulation and moisture flux over the Arctic. *Philosophical Transactions of the Royal Society of London*, **352**, 215–225.
- SERREZE, M. C., WALSH, J. E., CHAPIN, F. S., OSTERKAMP, T., DYURGEROV, M., ROMANOVSKY, V., OECHTEL, W. C., MORISON, J., ZHANG, T., and BARRY, R. G., 2000, Observational evidence of recent change in the northern high-latitude environment. *Climatic Change*, **46**, 159–207.
- SHENG, Y., SMITH, L. C., FREY, K. E., and ALSDORF, D. E., 2002, A high temporal resolution data set of ERS scatterometer radar backscatter for research in Arctic and sub-Arctic regions. *Polar Record*, **38**, 115–120.
- SHOKR, M. E., and BARBER, D. G., 1994, Temporal evolution of physical and dielectric properties of sea ice and snow during the early melt season: observations from SIMS '90 experiment. *Journal of Glaciology*, **40**, 16–30.
- SNYDER, J. A., MACDONALD, G. M., FORMAN, S. L., TARASOV, G. A., and MODE, W. N., 2000, Postglacial climate and vegetation history, north-central Kola Peninsula, Russia: pollen and diatom records from Lake Yarnyshnoe-3. *Boreas*, **29**, 261–271.
- TAO, X., WALSH, J. E., and CHAPMAN, W. L., 1996, An assessment of global climate model simulations of arctic air temperatures. *Journal of Climate*, **9**, 1060–1076.
- ULABY, F. T., MOORE, R. K., and FUNG, A. K., 1982, *Microwave Remote Sensing*, volumes 1, 2 and 3 (Massachusetts: Addison-Wesley).
- VINNIKOV, K. Y., ROBOCK, A., STOUFFER, R. J., WALSH, J. E., PARKINSON, C. L., CAVALIERI, D. J., MITCHELL, J. F. B., GARRETT, D., and ZAKHAROV, V. F., 1998, Global warming and Northern Hemisphere sea ice extent. *Science*, **286**, 1934–1937.
- WALKER, H. J., 1998, Arctic deltas. *Journal of Coastal Research*, **14**, 718–738.
- WEAVER, A. J., BITZ, C. M., FANNING, A. F., and HOLLAND, M. M., 1999, Thermohaline circulation: high-latitude phenomena and the difference between the Pacific and Atlantic. *Annual Review of Earth and Planetary Sciences*, **27**, 231–285.
- WINEBRENNER, D. P., NELSON, E. D., and COLONY, R., 1994, Observations of melt onset on multiyear Arctic sea ice using the ERS 1 synthetic aperture radar. *Journal of Geophysical Research*, **99**, 22 425–22 441.
- WISMANN, V., 1998, Land surface monitoring with spaceborne scatterometers. *Proceedings of a Joint ESA–Eumetstat Workshop on Emerging Scatterometer Applications—from Research to Operations, 5–7 October 1998* (Noordwijk, The Netherlands: ESA), pp. 25–31.
- WOHL, G. M., 1995, Operational sea ice classification from synthetic aperture radar imagery. *Photogrammetric Engineering and Remote Sensing*, **61**, 1455–1462.
- YE, H. C., 2000, Decadal variability of Russian winter snow accumulation and its associations with Atlantic sea surface temperature anomalies. *International Journal of Climatology*, **20**, 1709–1728.
- YUEH, S. H., and KWOK, R., 1998, Arctic sea ice extent and melt onset from NSCAT observations. *Geophysical Research Letters*, **25**, 4369–4372.